A plastic-damage constitutive model for the finite element analysis of fibre reinforced concrete

Iulia C. Mihai[1*], Anthony D. Jefferson[1], Paul Lyons[2]

[1] Cardiff University, School of Engineering, Queen's Buildings, The Parade, CF24 3AA, UK

[2] LUSAS, www.lusas.com

* Corresponding author. Email: mihaiic1@cardiff.ac.uk

Keywords: fibre reinforced concrete (FRC); constitutive model; damage; plasticity; crack-bridging.

Abstract

A unique constitutive model for fibre reinforced concrete (FRC) is presented, which combines a number of mechanics-based sub models for the simulation of directional cracking, rough crack contact and the crack-bridging action of fibres. The model also contains a plasticity component to simulate compressive behaviour. The plasticity component employs a frictional hardening/softening function which considers the variation of compressive strength and strain at peak stress with fibre content. Numerical results from a range of single-point and finite element simulations of experimental tests show that the model captures the characteristic behaviour of conventional fibre reinforced concrete with good accuracy.

1. Introduction

The addition of randomly distributed short fibres in a cementitious matrix can significantly improve the fracture properties of these fibre reinforced cementitious composites (FRCC). For the moderate fibre percentages used in many commercial mixes (0.5-2% by volume), the uniaxial tensile and compressive strengths are only increased by a relatively small amount, but it is the overall toughness, energy absorption and crack width control characteristics that can be dramatically improved by the introduction of these fibres. The degree of this enhancement depends mainly on the content and geometry of the fibres as well as upon the fibre-concrete matrix bond properties. This substantial increase in toughness and fracture resistance derives from the debonding and pull-out of fibres from the cementitious matrix. The underlying failure mechanism of cementitious composites, reinforced with randomly oriented discontinuous fibres, is also largely governed by fibre pull-out. This may or may not be accompanied by fibre rupture, depending on the fibre geometry and fibre-cement matrix interface properties [1-3]. When a crack opens, the fibres crossing the crack plane begin to debond and are subsequently pulled out (i.e. the fibres slide relative to the concrete matrix). In this process, they can be considered to apply closure tractions to the crack faces thus stabilising the crack growth. Via these crack-bridging mechanisms, the fibres continue to transfer stresses between the two crack faces until their complete pull-out.

Several models that describe the pull-out of randomly distributed short fibres from a cementitious matrix have been proposed [1,2,4-7]. Naaman et al. [4,5] investigated the influence of fibre-matrix bond properties on the behaviour of FRCCs using an analytical model, since it had become apparent from experimental investigations that the behaviour of FRC, particularly in the post-cracking stage, was strongly influenced by the interfacial bond-slip response. Assuming a linear-elastic – constant frictional bond-slip relationship they formulated a model that describes

the whole pull-out process of a single fibre aligned with the pull-out force. Li et al. [1], Li [2] and Lin and Li [7] derived a series of closed form analytical solutions that describe the pull-out of fibres that have 3-D uniform random distributions in location and orientation relative to the matrix crack plane. In these contributions, Li and co-workers considered a number of assumptions for the fibre-matrix bond model, including constant interface shear stress (pure frictional behaviour) [2] or slip-weakening [1] and slip-hardening behaviour [1,7]. The pull-out behaviour of steel hooked-end fibres has been addressed by Zhan and Meschke [8] who proposed an analytical model in which the anchorage effects induced by the hooks are evaluated at key pull-out stages. At each of these key stages, which depend on the geometrical configuration of the hooks, the resulting anchorage force was determined from equilibrium of forces and moments and taking into account the damage of concrete and the yielding steel.

Since the addition of fibres has a direct impact on cracking processes, their influence is more significant in tension than compression. Li and Li [9] proposed a model based on continuum damage mechanics for the tensile behaviour of fibre reinforced concrete. Lange-Kornback and Karihaloo [10] proposed a model which combined fracture mechanics and a statistical based fibre bridging approach to represent the softening tensile behaviour of FRC.

A number of macroscopic models have been proposed for simulating the compressive behaviour of FRCs; Bencardino et al. [11] provides a review of four empirical models for the stress-strain behaviour of steel fibre-reinforced concrete in compression [12-15] and compares their performance against several sets of experimental data. The study concludes that each of the models studied agrees well with the experimental data from which the model relations were derived but that the models do not show the same level of agreement when compared with other experimental data.

Macroscopic models often originate from models for plain concrete that have been modified or extended to describe FRC behaviour. They tend to make use of continuum damage and or plasticity theories and have an additional component that addresses the crack-bridging effect of fibres. Fanella and Krajcinovic [16] formulated a continuum damage model to simulate the compressive and tensile behaviour of FRC in which the damage functions for the cementitious matrix were coupled with those of the fibres in an equilibrium equation based on a parallel arrangement of the composite. Peng and Meyer [17] presented a continuum damage based model for FRC in which the influence of fibres was taken into account phenomenologically by modifying the damage evolution functions to account for the presence of fibres. Luccioni et al. [18] proposed a homogenization approach using a modified mixture theory to model steel fibre reinforced concrete (SFRC) as a composite material comprising a concrete matrix and fibres. The concrete matrix is characterised by a plasticity model whereas the steel fibres are modelled as orthotropic elasto-plastic inclusions that can debond and pull-out from the matrix. Fibre debonding and slipping relative to the matrix is addressed through a fibre pull-out model component based on the work on Naaman et al [4,5] and Chanvillard [19]. Hameed et al. [20] combined an anisotropic damage-plasticity model for plain concrete with a constitutive law that modelled the damage of the fibre-matrix bond. In this formulation the damage of the fibre-matrix bond was described by a Weibull-type function.

The series of microplane models for plain concrete, developed since the mid 80s by Bažant and co-workers, has more recently been extended by Beghini et al. [21] and Caner et al. [22] for the case of fibre reinforced concrete. To include the effect of fibres bridging an open crack, the softening function of the concrete matrix was coupled in parallel with another cohesive relationship based on the load resistance model for steel fibre reinforced concrete of Kholmyansky [23] to give the evolution of the normal component of the microplane stress.

Formulations that model the fibres in a discrete manner have also been proposed. Radtke et al. [24] presented a framework that combined a damage model with a component that simulated fibre bridging forces. In this approach the matrix material was characterized by a regularised damage model and represented by a background mesh. Fibres are then considered as discrete entities, however they are not explicitly discretized; instead, reaction forces from the fibres to the matrix, named fibre-forces, are applied to the background mesh, at the points representing the ends of the fibres. The fibre-matrix interface behaviour obtained from experimental tests is used directly by assuming the fibre pull-out forces to be equal to the fibre forces applied on the background mesh.

A number of lattice models for fibre reinforced concrete have been proposed in recent years [25-28]. These models are successful at capturing both the complex mesostructure and the physical mechanisms that occur in such a composite as well as the overall macroscopic behaviour. However, the high computational cost of such models is still one of the major obstacles to them being applied extensively in the analysis of large scale structural elements. However, such models are very useful for enhancing our understanding of the mechanisms that govern FRC behaviour.

A rather different approach was more recently adopted by Oliver et al. [29] who proposed a micromorphic model that describes FRC as a combination of three constitutive domains: the concrete matrix, the fibres and the fibre-matrix interface. The model is formulated in the general framework of multifield theory and uses a morphological kinematic descriptor that directly characterizes the fibre-matrix bond slip mechanism. Micromorphic models can be generally classed as macroscopic models but enhanced with information coming from particle interactions occurring at lower scales.

In the present work a novel model for fibre reinforced concrete is presented that builds on an existing damage-plasticity-contact model for plain concrete proposed by Jefferson [30-31]. This model employs a number of mechanics-based sub models for the simulation of directional cracking, rough crack contact and the crack-bridging action of fibres. There was considerable new work involved in (i) adapting a scalar crack-bridging model to make it compatible with the damage-contact crack plane model; (ii) developing new expressions for the compressive behaviour of FRC for use in the plasticity model component; (iii) developing a robust consistent algorithmic tangent and stress-recovery approach for the combined plastic-damage-contact- fibre-bridging model; (iv) implementing the model in a finite element code in a computationally robust manner and; (v) validating the model using a range of experimental data. The result of this work is a new finite element material model that is applicable to a wide range of FRC problems and allows the effective simulation of a wide range of FRC characteristic behaviour.

The remainder of the paper is arranged as follows:

Section 2 presents a crack plane sub-model for the crack-bridging action of short fibres embedded in a concrete matrix and describes how this is included in a damage-contact crack plane formulation;

Section 3 provides details of how the combined crack plane sub-model is implemented in the model of Jefferson [30] that considers cracks that can form and grow in multiple directions;

Section 4 describes the plasticity component of the model that simulates the variation of compressive behaviour with fibre content;

Section 5 presents the consistent tangent matrix / stress recovery algorithm and describes how the model was implemented in a finite element code;

In Section 6 a set of single-point simulations of uniaxial tension and compression experiments is presented followed by results from finite element simulations of

experimental tests on steel fibre reinforced concrete beams with and without additional longitudinal reinforcement.

2. Description of the model

2.1. Preliminaries and problem statement

Conventional FRC normally has a volume fraction of fibres in the range 0.5-2%, although mixes with up to 6% have been used. FRC specimens subjected to tensile loading typically show an increase in the tensile strength and toughness (generally measured as fracture energy) of the composite with increasing fibre content [32,33]. The mechanical properties of the composite also depend on the properties of the matrix, on the properties and geometry of the fibres and upon the characteristics of the fibre-matrix interface and the methods of processing.

The aim of the present work was to develop a robust and accurate constitutive model which is able to represent the characteristic behaviour of cementitious composites reinforced with randomly distributed short fibres – in particular steel fibres – and which is suitable for implementation in a commercial finite element code. The robustness, accuracy and ease of use of the model are considered to be equally important.

The constitutive model is developed in the plastic-damage-contact (p-d-c) framework previously proposed by Jefferson [30,31] in the Craft model for plain concrete which is extended here to address FRC behaviour. A particular aspect of the original Craft model is its ability to simulate multiple embedded cracks with various orientations, also referred to as crack planes. Such a feature proves to be advantageous when modelling fibre reinforced concrete since the bridging action of fibres across a crack plane has a major influence on the cracking behaviour and enhances overall ductility. Therefore it is the crack plane behaviour that drives the overall behaviour of the composite.

2.2. Crack plane formulation

In this work, a crack plane is defined as the mid surface of a narrow band of material of width h containing a crack (or micro-cracks). The orientation of the plane is defined by axes $\mathbf{r}_i$ (i=1 to 3), with unit vector $\mathbf{r}_1$ being the normal to the crack plane and $\mathbf{r}_2$ and $\mathbf{r}_3$ being orthogonal in-plane unit vectors (Figure 1). The components of the crack plane tractions ($\tilde{\boldsymbol{\sigma}}$) and relative-displacement vector ($\tilde{\mathbf{u}}$) are as follows:

$$\tilde{\boldsymbol{\sigma}} = \begin{bmatrix} \tilde{\sigma}_{11} & \tilde{\sigma}_{12} & \tilde{\sigma}_{13} \end{bmatrix}^{\mathrm{T}} \text{ and } \tilde{\mathbf{u}} = \begin{bmatrix} \tilde{u}_1 & \tilde{u}_2 & \tilde{u}_3 \end{bmatrix}^{\mathrm{T}} \quad (1)$$

Crack plane quantities are also referred to as local quantities, such that the subscripts 1 to 3 in equation 1 relate to the directions $\mathbf{r}_1$ to $\mathbf{r}_3$. The width of the crack band may be associated with the width of a fracture process zone [34]. The inelastic components of the crack-plane-relative-displacements and crack-plane-strains are related by the equation $\breve{\boldsymbol{\varepsilon}} = \frac{1}{h}\breve{\mathbf{u}}$ and the elastic crack plane constitutive relationship is given by:

$$\tilde{\boldsymbol{\sigma}} = \tilde{\mathbf{D}}\ \tilde{\boldsymbol{\varepsilon}}_{\mathrm{e}} = \tilde{\mathbf{D}}\ \left(\tilde{\boldsymbol{\varepsilon}} - \breve{\boldsymbol{\varepsilon}}\right) \quad (2)$$

in which $\tilde{\boldsymbol{\varepsilon}}_{\mathrm{e}}$ = elastic crack-band strain vector, $\breve{\mathbf{u}}$ = inelastic component of the relative-displacement vector, $\breve{\boldsymbol{\varepsilon}}$ = inelastic or 'fracture' strain vector, that is related to the deformations due to cracking. The inelastic strain tensor in Cartesian coordinates is often expressed in the form

$\breve{\boldsymbol{\varepsilon}}_{xyz} = {}^{1}\!/_{2h}\left[\mathbf{r}\otimes\breve{\mathbf{u}}_{xyz} + \breve{\mathbf{u}}_{xyz}\otimes\mathbf{r}\right]$, which is equivalent to our transformed inelastic strain vector $\breve{\boldsymbol{\varepsilon}}_{\mathrm{xyz}} = \mathbf{N}^{\mathrm{T}}\ \breve{\boldsymbol{\varepsilon}}$. $\mathbf{N}$ is a stress transformation matrix relating local to Cartesian stresses, $\mathbf{N}^{\mathrm{T}}$ gives the required strain transformation and $\breve{\mathbf{u}}_{xyz}$ is a Cartesian vector of inelastic relative displacements. It will be seen later on in this paper (in equation 19) that the sum of the inelastic strains of all cracks at a point form the summed fracture strain vector. The scalar magnitude of the inelastic relative-displacement is denoted $\breve{u}$ and the associated strain measure $\breve{\varepsilon}$.

$\tilde{\mathbf{D}} = E\cdot\begin{bmatrix} 1 & 0 & 0 \\ 0 & \dfrac{1}{2(1+\nu)} & 0 \\ 0 & 0 & \dfrac{1}{2(1+\nu)} \end{bmatrix}$ is the elasticity tensor of the crack plane, where E and ν are Young's modulus and Poisson's ratio of the FRC respectively. It is assumed that Poisson's ratio of the composite is the same as that of the plain concrete matrix, i.e. $\nu = \nu_m$.

When the model is applied to continuum elements, h is not used directly to relate relative displacements to strains. Instead, the crack-band model of Bazant and Oh [34] is used in which the inelastic local strains depend upon the element characteristic length (ℓ_{ch}) and the fracture energy parameter (G_f).

The effect of fibres on the (effective) elastic modulus of the composite is taken into account according to the law of mixtures, with the fibre component being derived from a three-dimensional random fibre network as presented in Garg et al. [35]:

$$E = \frac{E_f V_f}{6} + E_m\left(1 - \frac{V_f}{6}\right) \tag{3}$$

in which E_f and E_m are the Young's moduli of the fibre and the cementitious matrix respectively and V_f is the volume fraction of the fibres. It is noted that the addition of fibres in relatively limited amounts, as is the case for conventional FRC, has a second order effect on the effective elastic properties. This has been demonstrated in a study on the effective elastic properties of fibre reinforced cementitious composites that used continuum micromechanics and finite element predictions [36].

The degree of damage on the crack plane is characterised by a damage variable, $\omega \in [0,1]$. Making use of this damage variable, Eq. 2 can be written as:

$$\tilde{\boldsymbol{\sigma}} = (1-\omega)\,\tilde{\mathbf{D}}\,\tilde{\boldsymbol{\varepsilon}} \tag{4}$$

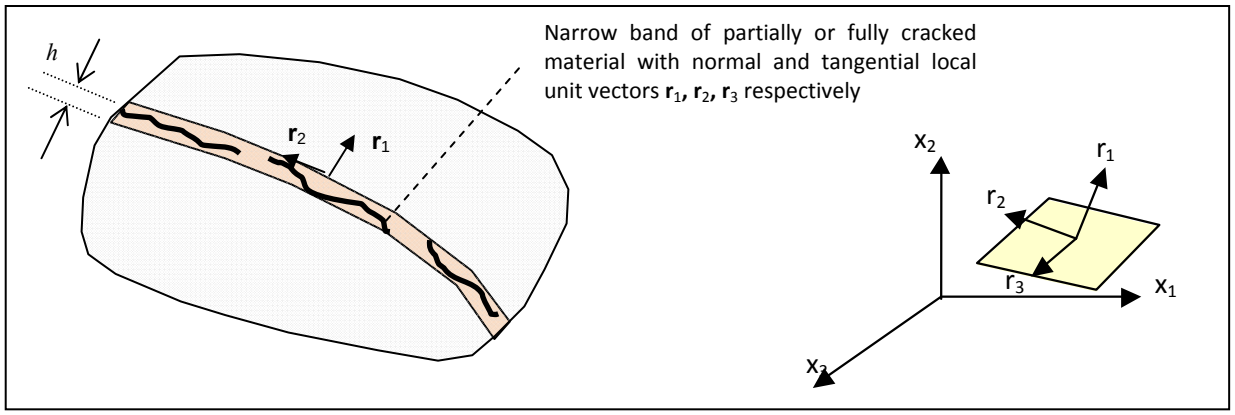

Figure 1. Schematic representation of the crack plane

Cracks are initiated when the macroscopic major principal stress exceeds the tensile strength of the matrix. Once formed, the fibres that cross the crack start to exert a crack bridging action as they pull out from the matrix. Tensile and/or shear stresses are transferred across the crack plane through the intact material and through the bridging action of the fibres. The model makes use of the following assumptions in characterising the crack plane behaviour.

1. Fibre bridging becomes active once damage is initiated (i.e. when $\omega>0$).
2. The bridging action of fibres is active only on the damaged proportion of a crack plane (i.e. on ω) as illustrated in Figure 2.
3. Fibre rupture is not taken into account, since it is rarely relevant for steel-fibre cementitious composites.
4. The bending stiffness or dowel action of fibres is negligible.
5. Bridging fibres are assumed to deform in accordance with the relative crack displacements, as illustrated in Figure 3.

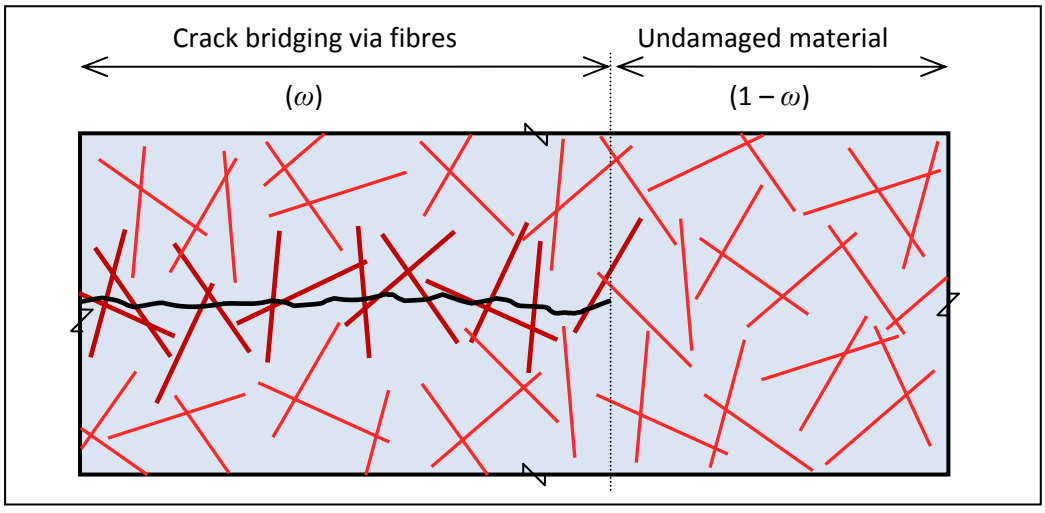

Figure 2. Stress transfer across crack plane assumption

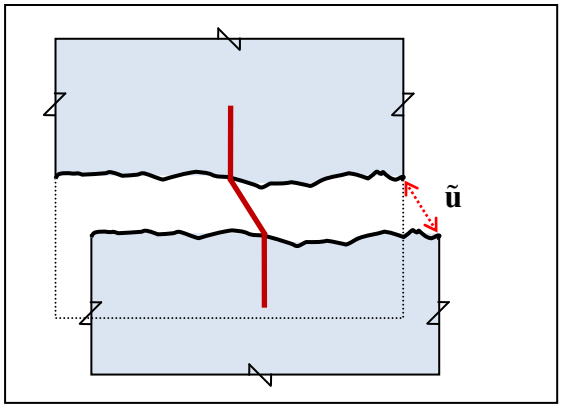

Figure 3. Schematic illustration of Assumption 4

The bridging action of fibres crossing a crack plane is interpreted in a classical damage form and the crack-bridging stress takes the form given in Eq. (5):

$$\tilde{\boldsymbol{\sigma}}_B = (1-\omega_f)\tilde{\mathbf{D}}_{sf}\tilde{\boldsymbol{\varepsilon}} \tag{5}$$

where ω_f is a fibre effective damage parameter.

Based on assumptions 4 and 5 $\tilde{\mathbf{D}}_{sf}$ can be written as $\tilde{\mathbf{D}}_{sf} = E_{sf}\cdot\mathbf{I}$, where $\mathbf{I}$ is the second order identity matrix and E_{sf} represents the effective elastic stiffness of the fibres crossing a crack plane before significant debonding occurs.

According to the first two assumptions, the stresses transferred across the crack plane through the intact material and through the bridging action of the fibres can then be expressed as:

$$\tilde{\boldsymbol{\sigma}} = (1-\omega)\tilde{\mathbf{D}}\,\tilde{\boldsymbol{\varepsilon}} + \omega(1-\omega_f)\tilde{\mathbf{D}}_{sf}\tilde{\boldsymbol{\varepsilon}} \tag{6}$$

The evolution of ω_f is based on the crack-bridging model of Lin and Li [7] in which the debonding phase is assumed to be linear elastic. The expression of the fibre effective damage parameter ω_f is evaluated using the 1D form of Eq. (5):

$$\omega_f = 1-\frac{\tilde{\sigma}_B}{E_{sf}\zeta_f} \tag{7}$$

in which ζ_f is an effective crack opening parameter that takes into account normal and shear crack opening components as follows:

$$\zeta_f = \frac{1}{2}\left(\tilde{\varepsilon}_{11} + \sqrt{\tilde{\varepsilon}_{11}^{\,2} + 4\left(\tilde{\varepsilon}_{12}^{\,2} + \tilde{\varepsilon}_{13}^{\,2}\right)}\right) \tag{8}$$

The fibre crack-bridging stress ($\tilde{\sigma}_B$) is based on the model of Li et al. [1] in which $\tilde{\sigma}_B$ is obtained by integrating the individual pull-out contributions of fibres crossing the crack plane:

$$\tilde{\sigma}_{\mathrm{B}}(\breve{u}) = \frac{V_f}{A_f}\int_{\varphi}\int_{z} P_f(\breve{u})\cdot p(\varphi)\cdot p(z)\,\mathrm{d}\varphi\,\mathrm{d}z \tag{9}$$

where A_f is the area of the fibre cross-section, P_f is the pull-out force carried by a single fibre, $\breve{u}$ denotes the crack opening, φ is the orientation angle of the fibre relative to the crack plane and z is the distance between the centroid of a fibre and the crack plane. $p(\varphi)$ and $p(z)$ denote probability density functions of the fibre orientation angle and centroidal distance to the crack plane respectively. It can be noted from Eqs. (4)-(8) that the bridging action of fibres given by the integration of the contributions of fibres from all possible orientations (Eq. 9) contributes to

both normal and shear components of the crack plane stress. A further point regarding Eq. (9) is that it places no restriction on the form of the probability functions and therefore the expression can accommodate non-uniform fibre distributions. In such cases, the resulting double integral can be solved numerically if a tractable analytical solution to (9) is not available. A similar procedure is employed by Soroushian and Lee [37] to derive a theoretical expression for the number of fibres per unit cross-sectional area. Assuming a linear hardening relationship between the fibre-matrix interfacial shear stress (τ) and interfacial slip (S) respectively, Lin and Li [7] derived the pull-out force carried by a single fibre.

$$\tau = \tau_0 \left(1 + \beta_f \frac{S}{d_f} \right) \tag{10}$$

where d_f is the diameter of the fibre and τ_0 and β_f are material parameters that characterize the fibre-matrix interface; the former being the frictional sliding shear stress at the end of debonding stage and the latter a non-dimensional frictional sliding hardening parameter.

Considering the particular case of uniform random fibre distributions (i.e. $p(\varphi) = \sin\varphi$ and $p(z) = 2/L_f$), and by taking into account the snubbing effect of fibres, Lin and Li obtained the following analytical expression for $\tilde{\sigma}_B$;

$$\tilde{\sigma}_B = \sigma_0 (1 + c_f \eta_\varepsilon)(1 - \eta_\varepsilon)^2 \tag{11}$$

in which $\sigma_0 = g \tau_0 V_f (1 + \eta) \frac{L_f}{2 d_f}$, $c_f = \frac{\beta_f L_f}{2 d_f}$ and $\eta_\varepsilon = \frac{\zeta_f - \varepsilon_{0d}}{\varepsilon_{0p} - \varepsilon_{0d}}$. L_f is the fibre length, $g = \frac{2}{4 + f^2}\left(1 + e^{0.5\pi f}\right)$ is a factor that accounts for the snubbing effect with f being the snubbing coefficient and $\eta = \frac{V_f E_f}{(1 - V_f) E_m}$. $\varepsilon_{0d} = \frac{\tilde{u}_{0d}}{h}$ and $\varepsilon_{0p} = \frac{\tilde{u}_{0p}}{h}$, where $\tilde{u}_{0d}$ and $\tilde{u}_{0p}$ are the crack openings at the end of debonding and pull-out stage respectively, as given by Eqs. (12a,b):

$$\tilde{u}_{0d} = \frac{2 d_f}{\beta_f} \lambda \text{ and } \tilde{u}_{0p} = \alpha_p \frac{L_f}{2} \tag{12a,b}$$

where $\lambda = \cosh\left(\frac{\Omega L_f}{2 d_f} \right) - 1$ and $\Omega = \sqrt{4(1 + \eta)\beta_f \tau_0 / E_f}$. α_p in Eq. (12b) is a reduction coefficient that accounts for the fact that, for inclined fibres, the final pull-out distance is less than the embedment length, as reported by Naaman and Shah [38]. According to their experimental results, the final pull-out distance – defined as the total amount of observed slip at which the pull-out load drops to zero – decreases by approximately 20% relative to the embedment length, as the inclination angle increases. α_p is therefore taken as 0.8. The effective elastic stiffness of the fibres crossing the crack plane is then evaluated as $E_{sf} = \sigma_0 / \varepsilon_{0d}$. The fibre end slip ($S$) in Eq. (10) is directly related to ζ_f and therefore does not appear in the final Eq. (11).

The damage function that governs the crack plane cement-matrix damage parameter ω in Eq. (6), taken directly from [30], is written in terms of a crack plane effective damage strain parameter ζ and takes into account the normal and shear components of $\tilde{\boldsymbol{\varepsilon}}$. Full details of the damage function are given in Appendix A for completeness. We note that the length (h) used to relate the crack openings to their counterpart strain parameters is replaced by the element

characteristic length (ℓ_{ch}) when the model is implemented in a finite element program via the crack-band approach [34], as in the present work. To clarify the definition of ζ, we note that ζ is a function of $\tilde{\boldsymbol{\varepsilon}}$, $\tilde{\boldsymbol{\varepsilon}} = \tilde{\boldsymbol{\varepsilon}}_e + \breve{\boldsymbol{\varepsilon}}$ and $\breve{\boldsymbol{\varepsilon}} = {}^{1}\!/_{h}\,\breve{\mathbf{u}}$ (or $\breve{\boldsymbol{\varepsilon}} = {}^{1}\!/_{\ell_{ch}}\,\breve{\mathbf{u}}$ in the FE code). Thus, ζ depends on a local strain vector that includes both elastic and inelastic components, whereas it is only the inelastic strain that is scaled by the element characteristic length. The advantage of this approach is that our damage function is not of zero size (with undefined gradients) at damage initiation, which would be the case if it were defined in terms of the inelastic strain components alone.

2.3. Modelling different types of fibres

Various types of fibres, including steel, glass, synthetic and natural fibres are used in fibre reinforced cementitious composites. Regarding the geometry, the most commonly used fibres are straight, hooked and crimped. By calibrating the bond parameters of the model using the pull-out properties of single fibres, it was found that the behaviour of both types of fibre could be reasonably represented.

3. Embedded fibre bridged crack planes in a 3D constitutive model

The fibre-bridging crack plane model presented in Section 2 could be readily adapted for an interface element or an element with embedded strong discontinuities by replacing the local strains in Eq. (6) with relative displacements and the elastic constitutive tensor to that applicable to the interface under consideration. In the present work, this model is implemented in a 3D constitutive model with embedded directional crack planes and applied to continuum finite elements. Details of how the crack plane fibre-bridging model is incorporated in the 3D constitutive model for plain concrete [30,31], are presented below. It is noted that the authors also applied the crack plane formulation to a 3D micromechanics-based constitutive model which will be described in a forthcoming publication. The crack plane model described here has a normal and two orthogonal in-plane shear components, as required for the representation of a crack in a three dimensional setting. The basic finite element implementation of the model is therefore 3D but we have also implemented the model for a range of 2D finite element elements, and in this case, the crack plane has only one shear component. Our approach may be described as an embedded smeared crack-band model, which employs fracture energy regularisation with a directionally dependent element characteristic length, for both 2D and 3D finite elements.

3.1. Contact model

Experiments in which cracks are opened under normal loading and which are subsequently subjected to shear deformation [39] show a definite point at which contact is regained. The work described in reference [40] demonstrated that the locus of these contact points could reasonably be represented by a conical shaped 'contact function' φ in $\tilde{\mathbf{u}}$ space. Furthermore, by assigning a normal and shear stiffness to the interface, the stress developed after contact could be based on the embedment displacement, defined as the nearest distance to the contact surface in $\tilde{\mathbf{u}}$ space. In this paper, the approach is developed in terms of the crack plane strains $\tilde{\boldsymbol{\varepsilon}}$ (Eq. 4) rather than relative-displacements since the model is to be applied to a smeared crack-band. A recent further development of this type of contact model [41] involved representing a crack surface with a range

of cones of different slopes and heights according to an experimentally established statistical distribution function.

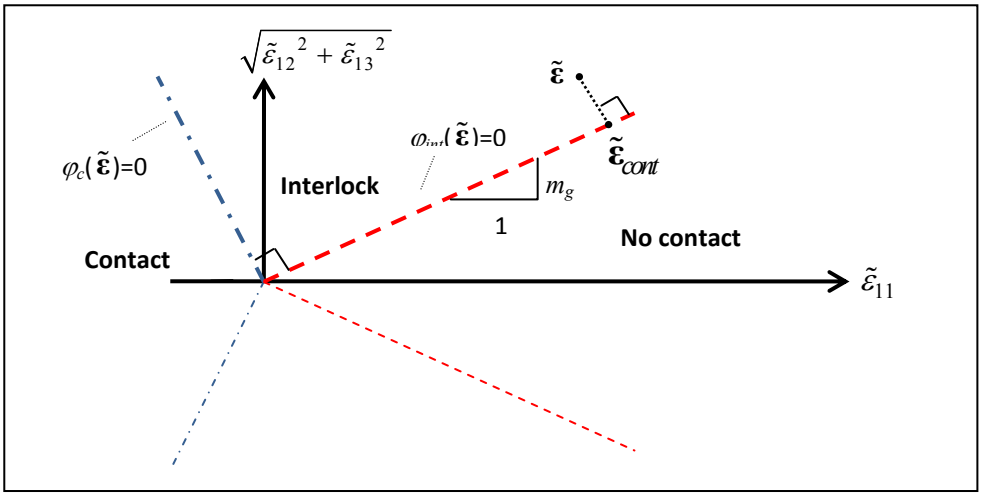

Figure 4. Contact function

A contact model similar to the one described in [30] was employed in this work. Two different contact surfaces, represented in Figure 4, are defined in the local strain space; an interlock contact surface (φ_{int}) and a closed contact surface (φ_c). The contact surfaces bound three regions corresponding to three contact states as follows:

$\varphi_{int}(\tilde{\boldsymbol{\varepsilon}}) \geq 0$ or $\tilde{\varepsilon}_{11} \geq \tilde{\varepsilon}_{ful}$ Open contact state (13a)

$\varphi_{int}(\tilde{\boldsymbol{\varepsilon}}) < 0$ and $\varphi_c(\tilde{\boldsymbol{\varepsilon}}) > 0$ Interlock contact state (13b)

$\varphi_c(\tilde{\boldsymbol{\varepsilon}}) \leq 0$ Closed contact state (13c)

where $\tilde{\varepsilon}_{ful}$ in (13a) denotes the crack opening beyond which no further contact can be gained in shear. The value of the limiting opening strain $\tilde{\varepsilon}_{ful}$ is taken from [30]; $\tilde{\varepsilon}_{ful} = m_{ful}\varepsilon_0$ where $\varepsilon_0 = u_0/h$ and u_0 is the relative displacement at the effective end of the uniaxial tensile softening curve ($u_0 \sim$ 0.2 for normal concrete). $m_{ful} \in [10,20]$ for concrete with relatively coarse aggregate particles, i.e. 20-30 mm and $m_{ful} \in [3,5]$ for concrete with relatively small coarse aggregate particles, i.e. 5-8 mm. Parameter m_{ful} was set to 5 for all numerical simulations presented here.

The interlock and closed surfaces delimitating the three contact regions are:

$$\varphi_{int}(\tilde{\boldsymbol{\varepsilon}}) = \frac{1}{\sqrt{1+m_g^{\,2}}}\left(m_g \cdot \tilde{\varepsilon}_{11} - \sqrt{\left(\tilde{\varepsilon}_{12}^{\,2}+\tilde{\varepsilon}_{13}^{\,2}\right)}\right) = 0 \qquad (14a)$$

$$\varphi_c(\tilde{\boldsymbol{\varepsilon}}) = \frac{1}{\sqrt{1+m_g^{\,2}}}\left(\tilde{\varepsilon}_{11} + m_g\sqrt{\left(\tilde{\varepsilon}_{12}^{\,2}+\tilde{\varepsilon}_{13}^{\,2}\right)}\right) = 0 \qquad (14b)$$

where m_g defines the slope of the interlock surface, as illustrated in Figure 4.

The two contact functions ($\varphi_*(\tilde{\boldsymbol{\varepsilon}})$) have the following properties:

$$\left|\frac{\partial \varphi_*}{\partial \tilde{\boldsymbol{\varepsilon}}}\right| = 1 \qquad (15a)$$

$$\varphi_*(\tilde{\boldsymbol{\varepsilon}})\frac{\partial \varphi_*}{\partial \tilde{\boldsymbol{\varepsilon}}} = \tilde{\boldsymbol{\varepsilon}} - \tilde{\boldsymbol{\varepsilon}}_{cont} \tag{15b}$$

where $\tilde{\boldsymbol{\varepsilon}}_{cont}$ is the local strain on the contact surface nearest to $\tilde{\boldsymbol{\varepsilon}}$, in local strain space (Figure 4).

The latter two properties are those of a signed distance function although here the properties are expressed in local strain rather than Cartesian space.

Considering the contact assumptions from [40], the stress transferred across the crack plane due to the crack faces regaining contact ($\tilde{\boldsymbol{\sigma}}_c$) depends upon the contact state as follows:

$$\tilde{\boldsymbol{\sigma}}_c = \tilde{\mathbf{D}}\,\tilde{\mathbf{e}}_c \tag{16a}$$

$$\tilde{\mathbf{e}}_c = \mathbf{0} \qquad \forall \quad \left(\varphi_{\text{int}}(\tilde{\boldsymbol{\varepsilon}}) \geq 0\right) \quad or \quad \left(\tilde{\varepsilon}_{11} \geq \tilde{\varepsilon}_{ful}\right) \tag{16b}$$

$$\tilde{\mathbf{e}}_c = H_c \varphi_{\text{int}}(\tilde{\boldsymbol{\varepsilon}})\frac{\partial \varphi_{\text{int}}}{\partial \tilde{\boldsymbol{\varepsilon}}} \qquad \forall \quad \left(\varphi_{\text{int}}(\tilde{\boldsymbol{\varepsilon}}) < 0\right) \quad and \quad \left(\varphi_c(\tilde{\boldsymbol{\varepsilon}}) > 0\right) \tag{16c}$$

$$\tilde{\mathbf{e}}_c = \tilde{\boldsymbol{\varepsilon}} \qquad \forall \quad \left(\varphi_c(\tilde{\boldsymbol{\varepsilon}}) \leq 0\right) \tag{16d}$$

where $\tilde{\mathbf{e}}_c$ is the local embedment strain and H_c in (16c) is a function that accounts for the fact that the contact potential reduces with crack opening. The reduction function derived by Mihai and Jefferson [42] from geometrical considerations was employed here:

$$H_c = e^{-3\frac{\tilde{\varepsilon}_{11}-\varepsilon_t}{\varepsilon_0}} \tag{17}$$

Including contact, the crack plane or local constitutive equation, Eq. (6) can be expressed as:

$$\tilde{\boldsymbol{\sigma}} = (1-\omega)\tilde{\mathbf{D}}\,\tilde{\boldsymbol{\varepsilon}} + \omega(1-\omega_f)\tilde{\mathbf{D}}_{\text{f}}\tilde{\boldsymbol{\varepsilon}} + \omega\,\tilde{\mathbf{D}}\,\tilde{\mathbf{e}}_{\text{c}} \tag{18}$$

The overall stress–strain relationship may be written as follows:

$$\boldsymbol{\sigma} = \mathbf{D}_e\left(\boldsymbol{\varepsilon} - \sum_{j=1}^{n_p}\mathbf{N}_j{}^T\breve{\boldsymbol{\varepsilon}}_j\right) \tag{19}$$

where $\breve{\boldsymbol{\varepsilon}}_{\text{j}}$ denotes the fracture strains for crack j and n_p = number of crack planes at the current point (i.e. at a finite element integration point).

The crack plane model relationship in Eq. (18) is now written in the form of Eq. (20a), in which the crack-plane index (j) and all dependencies are omitted for clarity:

$$\tilde{\boldsymbol{\sigma}} = \tilde{\mathbf{D}}\left(\mathbf{M}_{\text{s}}\tilde{\boldsymbol{\varepsilon}} + \tilde{\boldsymbol{\varepsilon}}_{\text{c}}\right) + \tilde{\mathbf{D}}_{\text{f}}\mathbf{M}_{\text{f}}\tilde{\boldsymbol{\varepsilon}} \tag{20a}$$

or

$$\tilde{\boldsymbol{\sigma}} = \tilde{\mathbf{D}}_{\text{dfs}}\tilde{\boldsymbol{\varepsilon}} + \tilde{\mathbf{D}}\tilde{\boldsymbol{\varepsilon}}_{\text{c}} \tag{20b}$$

where $\mathbf{M}_{\text{s}} = (1-\omega)\mathbf{I}$, $\mathbf{M}_{\text{f}} = \omega(1-\omega_{\text{f}})\mathbf{I}$, $\tilde{\mathbf{D}}_{\text{dfs}} = \tilde{\mathbf{D}}\mathbf{M}_{\text{s}} + \tilde{\mathbf{D}}_{\text{f}}\mathbf{M}_{\text{f}}$, $\tilde{\boldsymbol{\varepsilon}}_c = \omega\tilde{\mathbf{e}}_c$ and $\mathbf{I}$ = identity matrix.

From Eqs. (2) and (20b) it may be deduced that the fracture strains are given by:

$$\breve{\boldsymbol{\varepsilon}} = \tilde{\boldsymbol{\varepsilon}} - \tilde{\mathbf{C}}\tilde{\boldsymbol{\sigma}} = \tilde{\mathbf{C}}_{\text{dfs}}\left(\tilde{\boldsymbol{\sigma}} - \tilde{\mathbf{D}}\tilde{\boldsymbol{\varepsilon}}_{\text{c}}\right) - \tilde{\mathbf{C}}\tilde{\boldsymbol{\sigma}} = \left(\tilde{\mathbf{C}}_{\text{dfs}} - \tilde{\mathbf{C}}\right)\tilde{\boldsymbol{\sigma}} - \tilde{\mathbf{C}}_{\text{dfs}}\tilde{\mathbf{D}}\tilde{\boldsymbol{\varepsilon}}_{\text{c}} \tag{21}$$

in which $\tilde{\mathbf{C}} = \tilde{\mathbf{D}}^{-1}$ and $\tilde{\mathbf{C}}_{\text{dfs}} = \left(\tilde{\mathbf{D}}\mathbf{M}_{\text{s}} - \tilde{\mathbf{D}}_{\text{f}}\mathbf{M}_{\text{f}}\right)^{-1} = \tilde{\mathbf{D}}_{\text{dfs}}{}^{-1}$

Using Eq. (21) in Eq. (19) and noting that $\boldsymbol{\sigma} = \mathbf{N}\,\tilde{\boldsymbol{\sigma}}$, gives:

$$\boldsymbol{\sigma} = \left(\mathbf{I} + \mathbf{D}_e \sum_{j=1}^{n_p} \mathbf{N}_j^T \left(\tilde{\mathbf{C}}_{dfs_j} - \tilde{\mathbf{C}}_j \right) \mathbf{N}_j \right)^{-1} \mathbf{D}_e \left(\left(\boldsymbol{\varepsilon} - \boldsymbol{\varepsilon}_p \right) + \sum_{j=1}^{n_p} \mathbf{N}_j^T \tilde{\mathbf{C}}_{dfs_j} \tilde{\mathbf{D}} \tilde{\boldsymbol{\varepsilon}}_{c_j} \right) \quad (22)$$

An expression for the fracture strains may be derived by introducing Eq. (20b) into Eq. (21) which leads to:

$$\breve{\boldsymbol{\varepsilon}} = \left(\tilde{\mathbf{C}}_{dfs} - \tilde{\mathbf{C}} \right) \left(\tilde{\mathbf{D}}_{dfs} \tilde{\boldsymbol{\varepsilon}} + \tilde{\mathbf{D}} \tilde{\boldsymbol{\varepsilon}}_c \right) - \tilde{\mathbf{C}}_{dfs} \tilde{\mathbf{D}} \tilde{\boldsymbol{\varepsilon}}_c \quad (23)$$

Rearranging Eq. (23) gives:

$$\breve{\boldsymbol{\varepsilon}} = \left(\mathrm{I} - \tilde{\mathbf{C}} \tilde{\mathbf{D}}_{dfs} \right) \tilde{\boldsymbol{\varepsilon}} - \tilde{\boldsymbol{\varepsilon}}_c \quad (23a)$$

The expression in (23a) can then be used in Eq. (19) to calculate the global stress.

4. Compressive behaviour. Plasticity component

A plasticity component based on that presented in [30] is included in the present work to describe the characteristics of FRC behaviour in compression. The original plasticity component employed a simplified version of the Willam and Warnke [43] smooth triaxial yield surface and frictional work-hardening/softening functions. This model provided an effective characterisation of the compressive behaviour of plain concrete which included; significant pre-peak non-linearity and post-peak softening, increased strength and ductility with triaxial confinement. A full description of the plasticity component is given in [30,31]; however, key equations are given in Appendix B for completeness. In the present work, the original plasticity model was adopted and modified to account for the changes in the characteristic compressive behaviour that occur with the addition of fibres, in particular steel fibres. Experiments on steel fibre reinforced concrete specimens subjected to uniaxial compression [15,44] indicate several characteristic features such as:

- Increased toughness or ductility with increased fibre content
- Increased compressive strength with increased fibre content
- Increased strain at peak stress with fibre content
- Decreased slope of the post-peak part of the stress-strain curve with increased fibre content at a constant aspect ratio of fibres
- Decreased slope of the post-peak part of the stress-strain curve with increased fibre aspect ratio for constant fibre content

The key equations for the plasticity component are given in Table 1 with the terms being fully explained in Appendix B:

Table 1. Plasticity component

$F(\boldsymbol{\sigma}, \mathrm{Z}(\kappa)) = \sqrt{J_2} \cdot A_r(\theta) + \left(\alpha + \frac{\gamma}{3} \right) \cdot I_1 \cdot \mathrm{Z} - f_c \cdot \mathrm{Z} \cdot (1 - \alpha)$	Yield function	(24)
$G(\boldsymbol{\sigma}, \mathrm{Z}(\kappa)) = \sqrt{J_2}\ A_r(\theta) + \left(\alpha + \frac{\gamma}{3} \right) I_1\ \mathrm{Z}\ \psi - f_c\ \mathrm{Z}\ \psi\ (1 - \alpha)$	Plastic potential	(25)
$\dot{\boldsymbol{\varepsilon}}_p = \frac{\partial G}{\partial \boldsymbol{\sigma}} \dot{\lambda}_{pl}$	Flow rule	(26)
$\dot{\kappa} = \mathrm{X}(\boldsymbol{\sigma}) \boldsymbol{\sigma}^T \dot{\boldsymbol{\varepsilon}}_p$	Hardening rule	(27)

The original friction hardening/softening function for Z employed in [30] is calibrated against a uniaxial compression stress-strain curve, which is controlled by the uniaxial compressive strength (f_c) and the strain at peak uniaxial compression (ε_c). This function for Z gives a smooth transition from pre to post peak behaviour, was modified in this work as follows:

$$Z = Z_0 + \left[\frac{(1-Z_0)}{a_c} \, e^{-c_{c1}\eta_c} - Z_0 \right] \left(1\text{-}e^{-c_{c2}\eta_c} \right) \tag{28}$$

where $\eta_c = \kappa/\kappa_p$; κ_p = value of κ at the peak yield surface position given by:

$$\kappa_p = f_c \left(0.72\varepsilon_c - \frac{f_c}{2E} \right) \tag{29}$$

To ensure that the peak occurs at Z = 1, the constants must satisfy the following relationships:

$$c_{c1} = \frac{c_{c2} \, e^{-c_{c2}}}{1-e^{-c_{c2}}} \cdot \frac{1-\mathrm{Z}_0}{1-\mathrm{Z}_0 e^{-c_{c2}}} \qquad \text{and} \qquad a_c = e^{-c_{c1}} \left(1-e^{-c_{c2}} \right) \cdot \frac{1-\mathrm{Z}_0}{1-\mathrm{Z}_0 e^{-c_{c2}}} \tag{30a,b}$$

Parameter c_{c2} controls the slope of the descending branch of the stress-strain curve. As mentioned above, in the case of steel fibre reinforced concrete, the post-peak slope of the compressive stress-strain curve decreases with increasing fibre content. To reflect this, c_{c2} is assumed to have the following nonlinear variation with respect to the volume fractions of fibres V_f:

$$c_{c2} = \alpha_1 - \alpha_2 \cdot \eta_{\mathrm{v}} (V_f)^{\alpha_3} \tag{31}$$

with $\eta_{\mathrm{v}} = \dfrac{V_f}{V_{f\ \mathrm{lim}}}$, where $V_{f\,lim}$ represents the upper limit of the volume fraction of fibres taken here as 8%. It was found that values of α_1 = α_3 = 0.1 and α_2 = 0.08 provided a good match to the experimental data of Marar et al. [44].

It is further assumed that the compressive strength (f_c) and the strain at peak stress (ε_c) in Eq. (29) are functions of fibre content and aspect ratio [15,44]. The variations of both f_c and ε_c with the volume fraction (V_f), and aspect ratio ($a_f = L_f/d_f$) of the fibres are governed by Eqs. (32) and (33) respectively and illustrated in Figures 5a and 5b :

$$f_{\mathrm{c}}(V_f, a_f) = f_{\mathrm{c0}} \cdot \left[1 + \lambda_{\mathrm{v}}(V_f) \cdot \lambda_{\mathrm{a}}(a_f) \right] \tag{32}$$

$$\varepsilon_{\mathrm{c}}(V_f, a_f) = \varepsilon_{\mathrm{c0}} \cdot \left[1 + \lambda_{\mathrm{v}\varepsilon}(V_f) \cdot \lambda_{\mathrm{a}\varepsilon}(a_f) \right] \tag{33}$$

in which f_{c0} is the uniaxial compressive strength of the unreinforced matrix (i.e. when V_f = 0%), $\lambda_{\mathrm{v}}(V_f) = \dfrac{e^{c_{v1}\eta_v(V_f)}}{c_{v2} + e^{c_{v1}\eta_v(V_f)}} - \dfrac{1}{c_{v2}+1}$, $\lambda_{\mathrm{a}}(a_f) = \eta_a(a_f)^{c_{a1}}$ and $\eta_a(a_f) = \dfrac{a_f - a_{f0}}{a_{f\,\mathrm{lim}} - a_{f0}}$. A_{f0} and $a_{f\,\mathrm{lim}}$ are the lower and upper limits of the fibre aspect ratio. For steel fibres, a_{f0} and $a_{f\,\mathrm{lim}}$ are taken as 20 and 100 respectively. Moreover, ε_{c0} is the uniaxial compressive strain at peak stress of the unreinforced matrix, $\lambda_{\mathrm{v}\varepsilon}(V_f) = c_{v\varepsilon 3} \left[\dfrac{e^{c_{v\varepsilon 1} \cdot \eta_v(V_f)}}{c_{v\varepsilon 2} + e^{c_{v\varepsilon 1} \cdot \eta_v(V_f)}} - \dfrac{1}{c_{v\varepsilon 2}+1} \right]$ and $\lambda_{\mathrm{a}\varepsilon}(a_f) = \eta_a(a_f)^{c_{a\varepsilon 1}}$.

The set of parameters given in Table 2 were found to provide a good match to experimental results.

Table 2. Plasticity parameters

c_{v1}	c_{v2}	c_{a1}	$c_{v\varepsilon 1}$	$c_{v\varepsilon 2}$	$c_{v\varepsilon 3}$	$c_{a\varepsilon 1}$
10	15	0.5	18	100	10	3

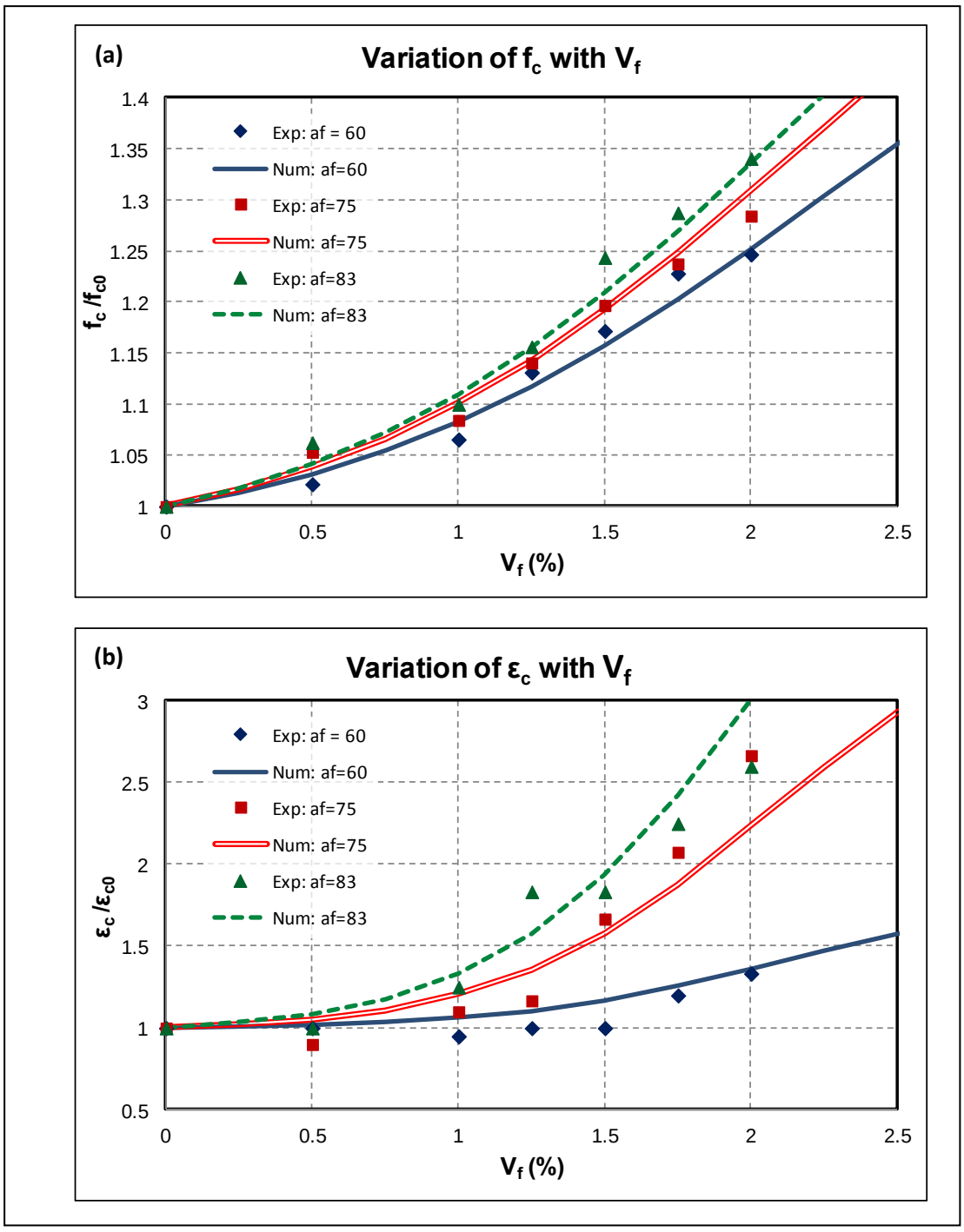

Figure 5. Variation of (a) the uniaxial compressive strength, f_c and of (b) the uniaxial compressive strain at peak stress, ε_c with fibre content, V_f.

5. Consistent tangent matrix

The derivation of the consistent tangent is given first for the case in which the plasticity component is not active.

The incremental crack plane relationships may be derived from Eq. (20a) to be:

$$\delta\tilde{\boldsymbol{\sigma}} = \tilde{\mathbf{D}}\left(\mathbf{M}_{\mathrm{s}} + \frac{\partial \mathbf{M}_{\mathrm{s}}}{\partial \tilde{\boldsymbol{\varepsilon}}} \circ \tilde{\boldsymbol{\varepsilon}} + \frac{\partial \tilde{\boldsymbol{\varepsilon}}_{\mathrm{c}}}{\partial \tilde{\boldsymbol{\varepsilon}}}\right)\delta\tilde{\boldsymbol{\varepsilon}} + \tilde{\mathbf{D}}_{\mathrm{f}}\left(\mathbf{M}_{\mathrm{f}} + \frac{\partial \mathbf{M}_{\mathrm{f}}}{\partial \tilde{\boldsymbol{\varepsilon}}} \circ \tilde{\boldsymbol{\varepsilon}}\right)\delta\tilde{\boldsymbol{\varepsilon}} = \left(\tilde{\mathbf{D}}\mathbf{M}_{\mathrm{s}}{}' + \tilde{\mathbf{D}}_{\mathrm{f}}\mathbf{M}_{\mathrm{f}}{}'\right)\delta\tilde{\boldsymbol{\varepsilon}} \tag{34}$$

in which $\circ$ denotes a third-order-matrix vector contraction. This can be re-written as:

$$\delta\tilde{\boldsymbol{\sigma}} = \tilde{\mathbf{D}}_{\mathrm{df}}{}'\delta\tilde{\boldsymbol{\varepsilon}} \tag{35}$$

where $\tilde{\mathbf{D}}_{\mathrm{df}}{}' = \tilde{\mathbf{D}}\mathbf{M}_{\mathrm{s}}{}' + \tilde{\mathbf{D}}_{\mathrm{f}}\mathbf{M}_{\mathrm{f}}{}'$

The incremental fracture strains are then given by Eq. (36):

$$\delta\breve{\boldsymbol{\varepsilon}} = \delta\tilde{\boldsymbol{\varepsilon}} - \tilde{\mathbf{C}}\delta\tilde{\boldsymbol{\sigma}} = \left(\tilde{\mathbf{D}}_{\mathrm{df}}{}'^{-1} - \tilde{\mathbf{C}}\right)\delta\tilde{\boldsymbol{\sigma}} = \left(\tilde{\mathbf{C}}_{\mathrm{df}}{}' - \tilde{\mathbf{C}}\right)\delta\tilde{\boldsymbol{\sigma}} = \tilde{\mathbf{C}}'\delta\tilde{\boldsymbol{\sigma}} \tag{36}$$

The incremental form of the constitutive relationship (19) (with $\boldsymbol{\varepsilon}_{\mathrm{p}} = 0$) is given by:

$$\delta\boldsymbol{\sigma} = \mathbf{D}_{\mathrm{e}}\left(\delta\boldsymbol{\varepsilon} - \sum_{\mathrm{j}=1}^{\mathrm{n_p}}\left(\mathbf{N}_{\mathrm{j}}{}^{\mathrm{T}}\delta\breve{\boldsymbol{\varepsilon}}_{\mathrm{j}} + \delta\mathbf{N}_{\mathrm{j}}{}^{\mathrm{T}}\breve{\boldsymbol{\varepsilon}}_{\mathrm{j}}\right)\right) \tag{37}$$

Using (36) in (37) and rearranging gives the following consistent incremental stress–strain relationship:

$$\delta\boldsymbol{\sigma} = \left(\mathbf{I} + \mathbf{D}_{\mathrm{e}}\left(\sum_{\mathrm{j}=1}^{\mathrm{n_p}}\mathbf{N}_{\mathrm{j}}{}^{\mathrm{T}}\tilde{\mathbf{C}}_{\mathrm{j}}{}'\mathbf{N}_{\mathrm{j}}\right)\right)^{-1}\mathbf{D}_{\mathrm{e}}\delta\boldsymbol{\varepsilon} \tag{38}$$

When the plasticity component is added, the consistent tangent matrix follows the same derivation as given in [30] and is included in Appendix C for completeness.

6. Numerical results

Numerical predictions from a range of single point and FE simulations are presented here to assess the performance of the proposed model.

A relatively small number of parameters are required by the model; apart from the parameters that are related to the behaviour of plain concrete, all of which are detailed in [30], the addition of fibres introduces a further seven parameters as follows:

- The modulus of elasticity for the fibre material E_f
- Fibre content, V_f and parameters relating to the geometry of fibres, L_f and d_f
- Parameters describing the fibre-matrix interface: β_f and τ_0
- Snubbing parameter f_{snub}

E_f, L_f and d_f can be obtained directly from material data sheets supplied by fibre manufacturers and V_f is specified in the mix design. The fibre-matrix interface parameters can be obtained from single fibre pull-out tests [7] whereas the snubbing parameter can be determined as proposed by Li et al. [45]. The parameters related to the plasticity component were fixed at the values given in Table 2 for all examples.

The sensitivity of the predicted response to variations in the fibre-matrix interface parameters is explored in the first example. No such study is performed for the other fibre parameters because these are based solely on the basic geometric and physical properties of the fibres themselves.

6.1. Single point simulations. Uniaxial tension test of Li et al. [33]

Numerical results for a uniaxial tension strain path obtained with the proposed constitutive model are compared with the experimental data of Li et al. [33] and presented in Figures 7a, b. Simulations for mixes with fibre volume fractions of 2%, 3% and 6% respectively were carried out for two different types of steel fibres, namely Dramix fibres– which have a circular cross-section and hooked ends – and Harex fibres – which have an arc cross-section and straight ends.

In the experimental tests, different concrete mixes were used for each fibre volume fraction in order to achieve sufficient workability: mix A was used for 2%, mix B for 3% and mix C for 6% fibre volume fraction respectively. Separate experimental tension tests were conducted on plain concrete specimens for all three plain mixes as well as on the associated FRC specimens. Therefore the numerical simulations were conducted in two stages as follows:

- Stage 1 comprised simulations of the uniaxial tension tests for the three plain concrete specimens, employing the material properties in Table 3. Comparisons between the numerical and experimental results are presented in Figure 6.
- Stage 2 simulations considered the fibre reinforced concrete specimens, using the material properties given in Tables 3 and 4. The predictive results for FRC using Dramix fibres are shown in Figure 7a and the results for FRC using Harex fibres are presented in Figure 7b.
-

Table 3. Material properties for plain concrete

Mix type	E_m [MPa]	ν	f_{c0} [MPa]	f_{t0} [MPa]	ε_{c0}	G_f [N/mm]
A	35000	0.18	46.3	3.6	0.003	0.08
B	32000	018	52.4	3.7	0.003	0.075
C	28000	0.18	52.2	3.9	0.003	0.065

f_{t0} – tensile strength of plain concrete (see Appendix A)

Table 4. Fibre properties

Fibre type	V_f (%)	Matrix type	L_f (mm)	d_f (mm)	E_f (MPa)	β_f	τ_0 (MPa)	f_{snub}
Dramix	2	A	30	0.5	200000	0.17	1.55	0.85
	3	B						0.8
	6	C						0.7
Harex	2	A	32	0.8	200000	0.105	2	0.85
	3	B						0.8
	6	C						0.7

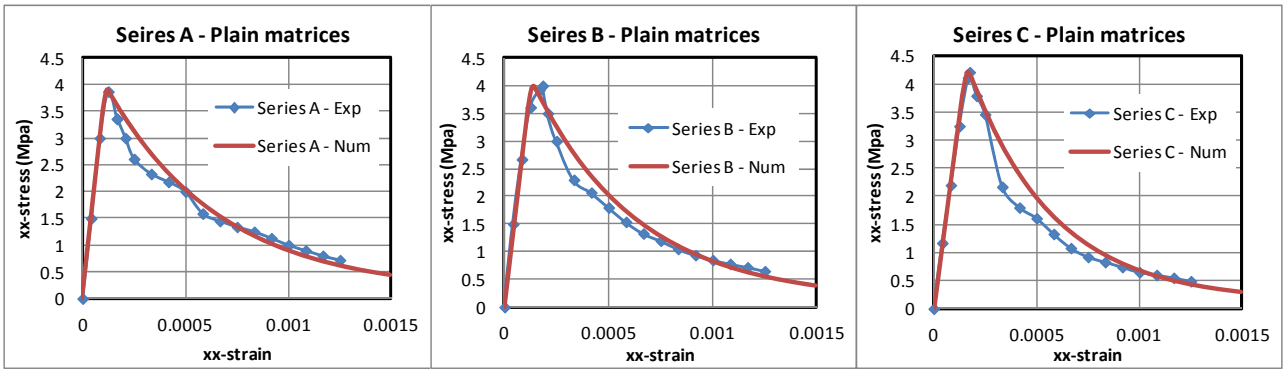

Figure 6. Numerical predictions for plain matrix. Uniaxial tension.

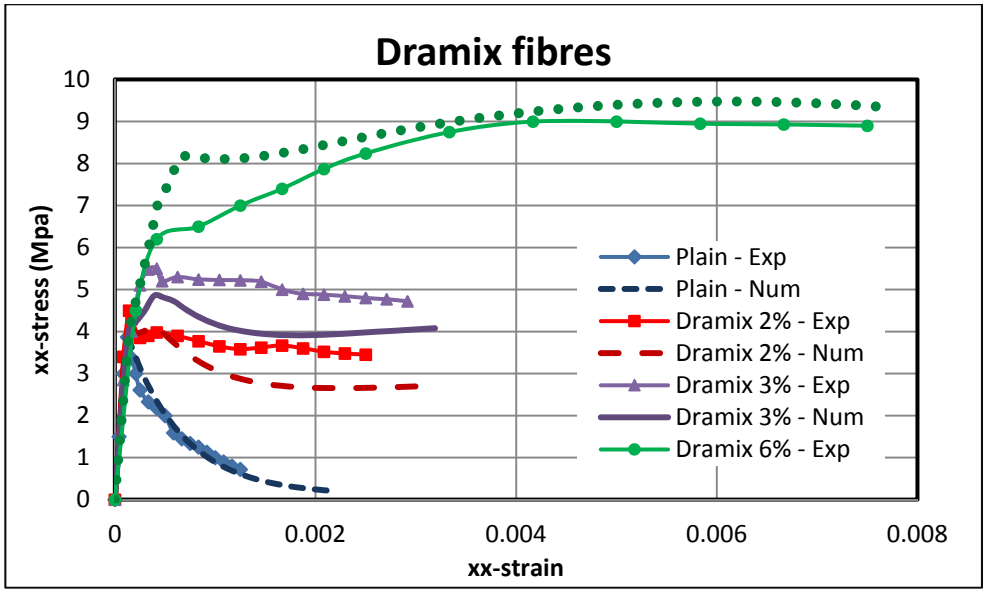

Figure 7a. Uniaxial tension predictions. Concrete reinforced with Dramix fibres

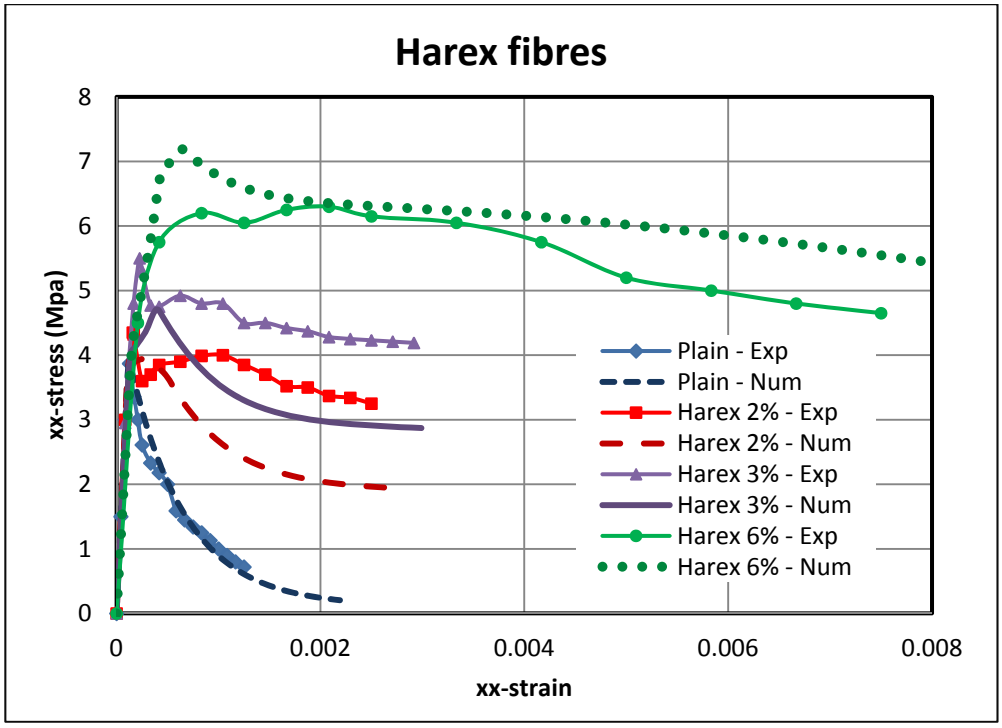

Figure 7b. Uniaxial tension predictions. Concrete reinforced with Harex fibres

It can be seen from Figures 7a and 7b that the model predicts well the characteristic increase of tensile strength and toughness with increasing fibre content. It is noted that only one experimental curve for each FRC mix was presented in Li et al. [33]. However, following an extensive experimental study on the behaviour of fibre reinforced concrete beams tested in 3-point bending, Parmentier et al. [46] reported a considerable variation of the mechanical performance, with experimental results from sets of tests with the same parameters having coefficients of variation greater than 20%. This level of experimental scatter was attributed to the heterogeneous nature of the material and was thought to depend mainly on variations in the distribution and orientation of fibres. Therefore, the apparent difference between the numerical predictions obtained with the proposed model and the experimental results is likely to be due to this inherent variability of FRC behaviour.

The sensitivity of the model to the fibre-matrix interface parameters τ_0 and β_f is shown in Figures 8a and 8b respectively for numerical simulations of uniaxial tensile tests using Dramix fibres with a volume fraction of 2%. In these simulations, the values used for τ_0 and β_f were varied by ± 20% relative to the nominal values from Table 4. The values of τ_0 and β_f employed for the sensitivity studies and the predicted strength values (f_{tf}), as well as those of the stress corresponding to a uniaxial tensile strain of 0.003 ($\sigma_{0.003}$), are given in Table 5. Values of the remaining parameters are those given in Table 4.

τ_0 has a moderate influence over the predicted values of strength, with a variation of under 5% between the strength values from simulation *S1* and simulation *S3* respectively. The influence of τ_0 is significantly stronger in the post peak region; the predicted values of $\sigma_{0.003}$ increase by approximately 35% as τ_0 increases from 1.25 in *S3* to 1.85 in *S1*.

The model sensitivity to the variation of β_f is altogether more limited; the predicted strength values remain unchanged whereas the predicted values of $\sigma_{0.003}$ increase by approximately 11% as β_f increases from 0.14 in *S6* to 0.2 in *S4*.

It is noted that values for the fibre-matrix interface parameters τ_0 and β_f can be obtained for single fibre pull-out tests [7].

Table 5. Sensitivity study. Fibre-matrix interface parameters

τ_0 sensitivity	V_f (%)	τ_0 [MPa]	β_f	f_{tf} [MPa]	$\sigma_{0.003}$ [MPa]
S1	2	1.85	0.17	4.18	3.18
S2		1.55		4.16	2.70
S3		1.25		4.10	2.20
β_f sensitivity	V_f (%)	τ_0 [MPa]	β_f	f_{tf} [MPa]	$\sigma_{0.003}$ [MPa]
S4	2	1.55	0.2	4.16	2.84
S5			0.17	4.16	2.70
S6			0.14	4.16	2.55

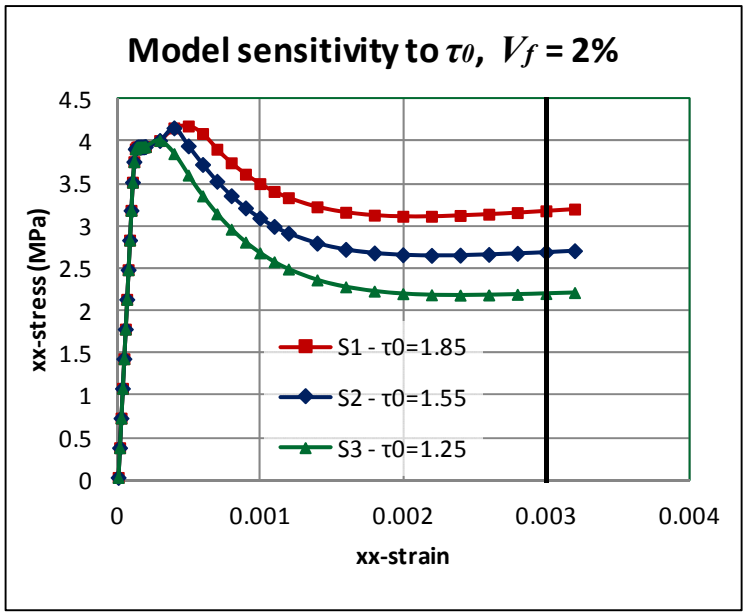

Figure 8a. Sensitivity of τ_0. Uniaxial tensile predictions

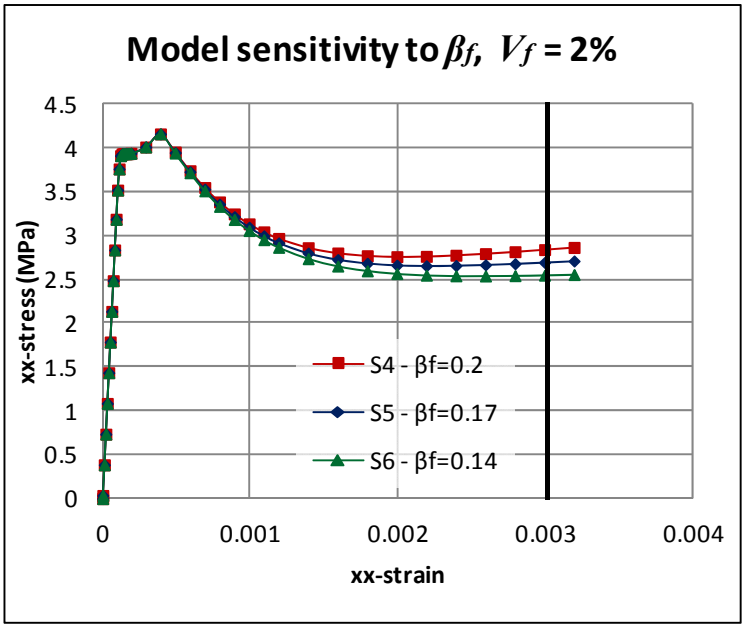

Figure 8b. Sensitivity of β_f. Uniaxial tensile predictions

6.2. Single point simulation. Uniaxial compression tests of Marar et al. [44]

In this example, results from single-point numerical predictions of uniaxial compression tests are compared with the experimental results of Marar et al. [44]. The experimental tests were performed on standard cylindrical specimens (150x300 mm) made of normal strength concrete reinforced with various volume fractions of hooked-end steel fibres of different aspect ratios. Simulations were carried out for two types of Dramix steel fibres; (i) L_f = 30 mm & d_f = 0.5 mm (i.e. aspect ratio of 60) and (ii) L_f = 50 mm & d_f = 0.6 mm (i.e. aspect ratio of 83). For each case, four different fibre volume fractions were considered; 0.5, 1.0, 1.5 and 2% respectively.

The values of the model parameters used in the numerical simulations are given in Table 6, and the predicted and experimental results are compared in Figures 9a and 9b.

Table 6. Material properties. Uniaxial compression simulations

E_m [MPa]	ν	f_{c0} [MPa]	f_{t0} [MPa]	ε_{c0}	G_f [N/mm]	E_f [MPa]	β_f	τ_0 (MPa)	f_{snub}
28000	0.18	52.2	3.9	0.002	0.065	200000	0.17	1.55	0.7

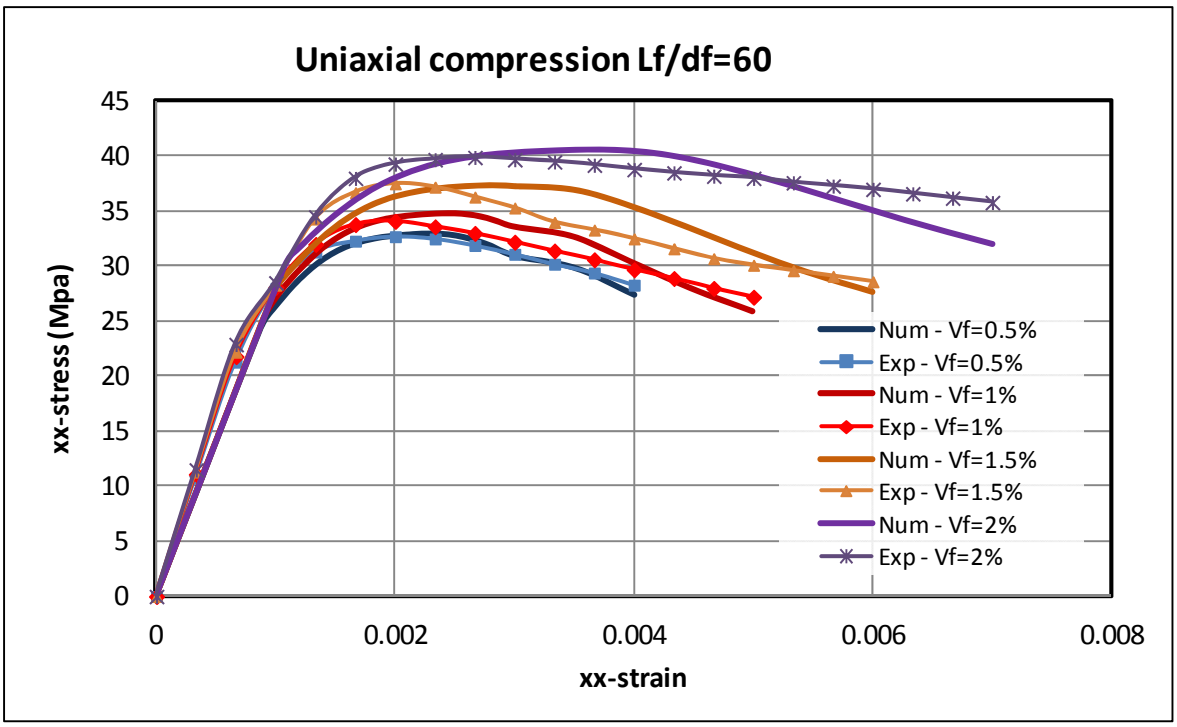

Figure 9a. Uniaxial compression predictions. (i) Fibre aspect ratio = 60

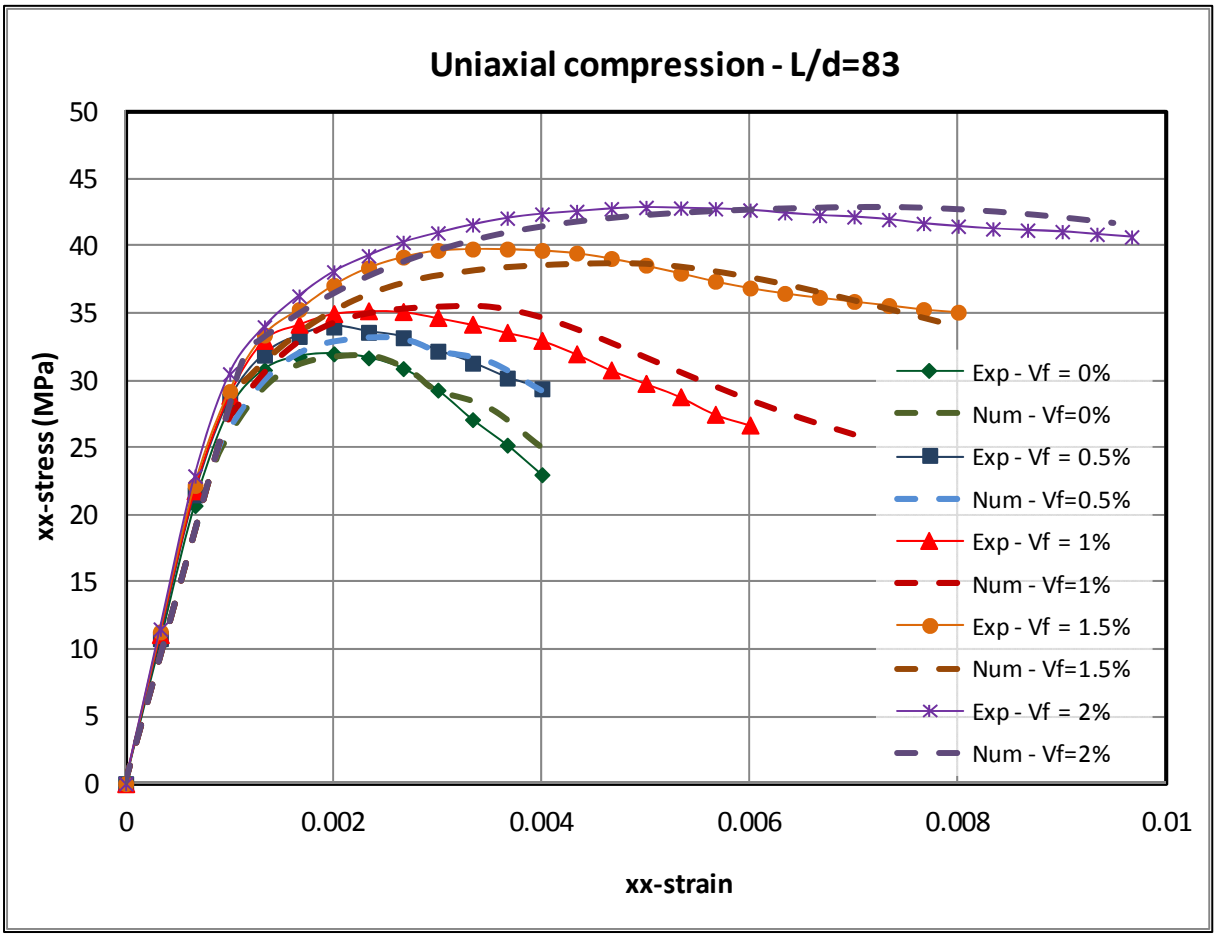

Figure 9b. Uniaxial compression predictions. (ii) Fibre aspect ratio = 83

Numerical predictions obtained for a substantial set of FRC mixes are in good agreement with experimental data; the model captures the increase of ductility in compression with increasing fibre content.

6.3. FE simulation. 3 point bend test of Bencardino et al. [47]

Both FE simulations were undertaken with the finite element program LUSAS in which the current model has been implemented. 4-noded linear quadrilateral elements with a 2x2 Gauss-Legendre integration rule were used throughout. The nonlinear solutions were undertaken with an incremental-iterative Newton solution scheme. The number of load/displacement increments for each solution varies from 30 to 70 and the convergence tolerance used was 0.01% for both the iterative displacement and out of balance force L2 norms.

In the first FE example, simulations of a series of 3-point bend tests by Bencardino et al. [47] are presented. The experimental tests were carried out on notched prismatic specimens made from plain concrete (PC) and steel fibre reinforced concrete (SFRC). Hooked-end Dramix steel fibres with volume fractions of 1% (DS1%) and 2% (DS2%) respectively were used. A schematic representation of the experimental set up as well as the specimen geometry and dimensions (in mm) are presented in Figure 10. Three specimens were tested in each set of experiments; however a single representative load-deflection curve per set was presented.

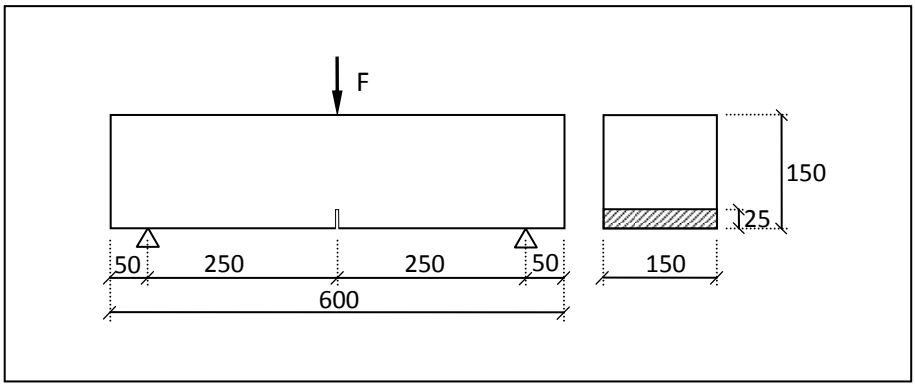

Figure 10. Bencardino et al. [47] experimental setup

The finite element mesh with the boundary conditions used for the numerical analysis is shown in Figure 11. The material parameters employed are given in Tables 7a and 7b. For each set of tests, finite element predictions of the load-central deflection curves (F-δ) are compared with the experimental curves (Figure 12). Plots of the major principal strains showing the regions of localised strains are presented on deformed meshes in Figures 13a,b. For convenience, the same strain range was used for all strain profiles in Figures 13a and b. The proposed model is able to capture the increase in strength and ductility of the composite as the fibre content increases. It is noted that significant scatter of the experimental post peak response has been reported by Bencardino et al. [47]. For instance, a coefficient of variation of the peak load of approximately 18% was obtained from the responses of the three specimens tested in the DS1% case. The scatter in the experimental results was attributed to an uneven fibre distribution. It can be observed from the FE strain profiles that damage is more localised for lower fibre volume content, as may be expected.

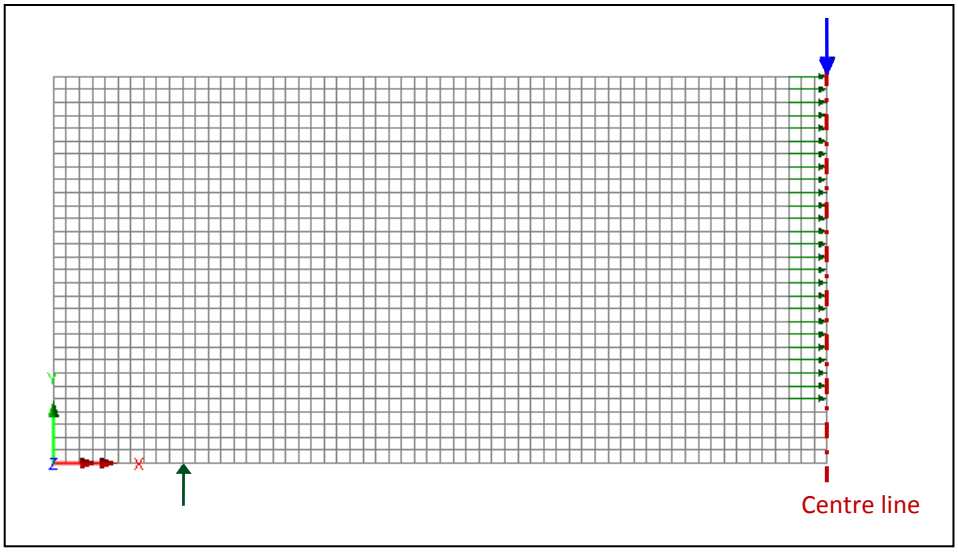

Figure 11. Finite element mesh and boundary conditions. Simulation of Bencardino et al. [47] experiment

Table 7a. Material properties for plain concrete

Case	E_m [MPa]	ν	f_{c0} [MPa]	f_{t0} [MPa]	ε_{c0}	G_f [N/mm]
PC	40000	0.2	68	2.5	0.002	0.07

Table 7b. Material properties for fibres

Case	V_f (%)	L_f (mm)	d_f (mm)	E_f (MPa)	β_f	τ_0 (MPa)	f_{snub}
DS1%	1	50	0.625	210000	0.06	1.9	0.85
DS2%	2						0.75

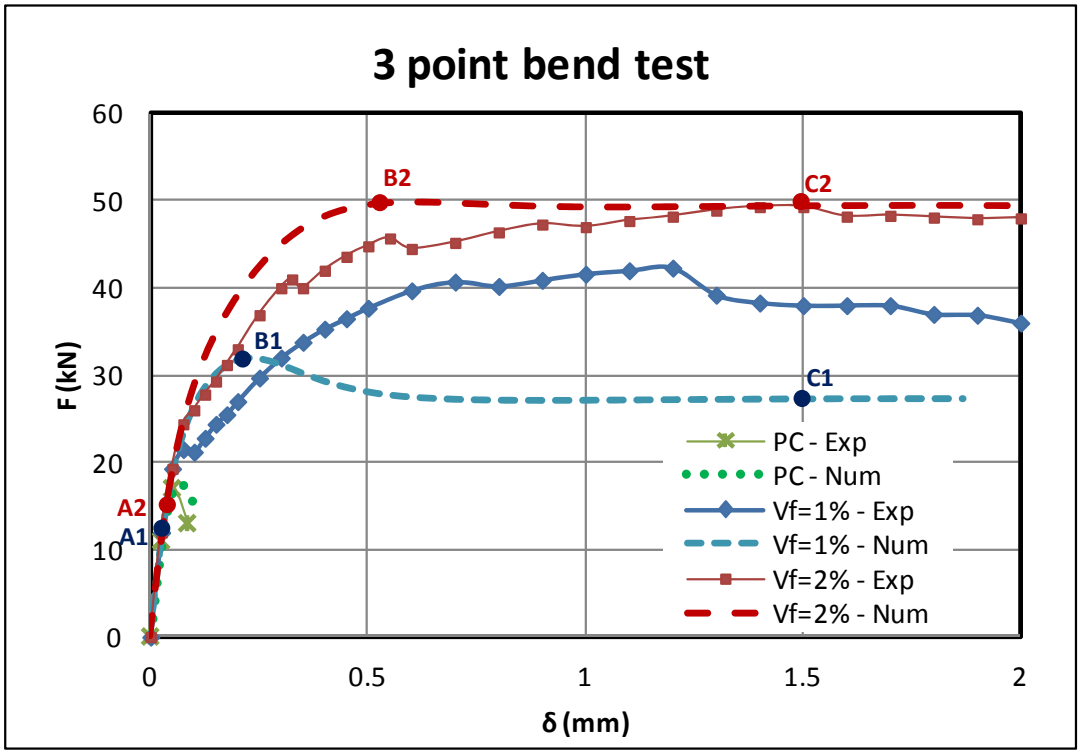

Figure 12. Load-displacement predictions from FE simulations of Bencardino et al. [47]

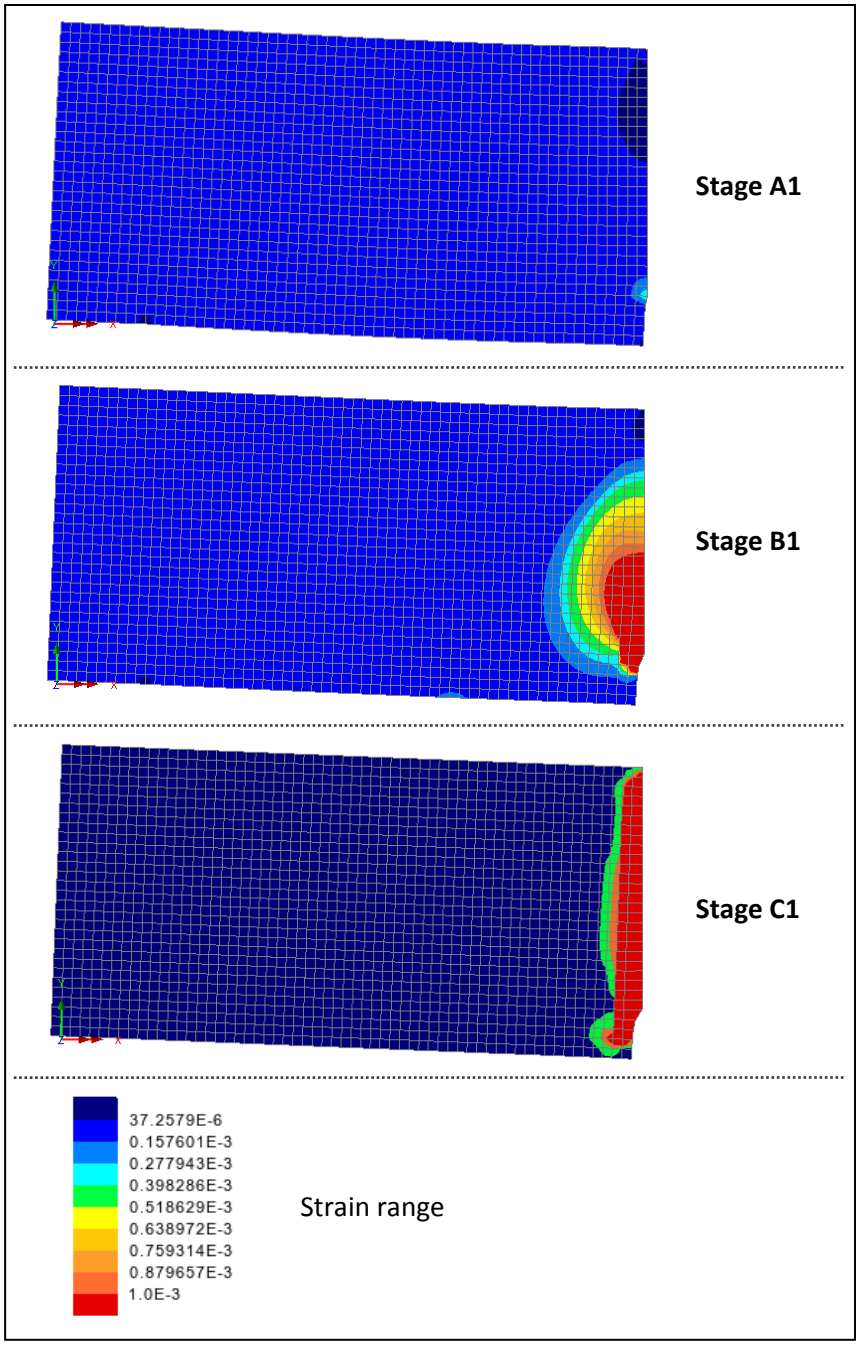

Figure 13a. Major principal strain profile from FE simulations. V_f = 1%

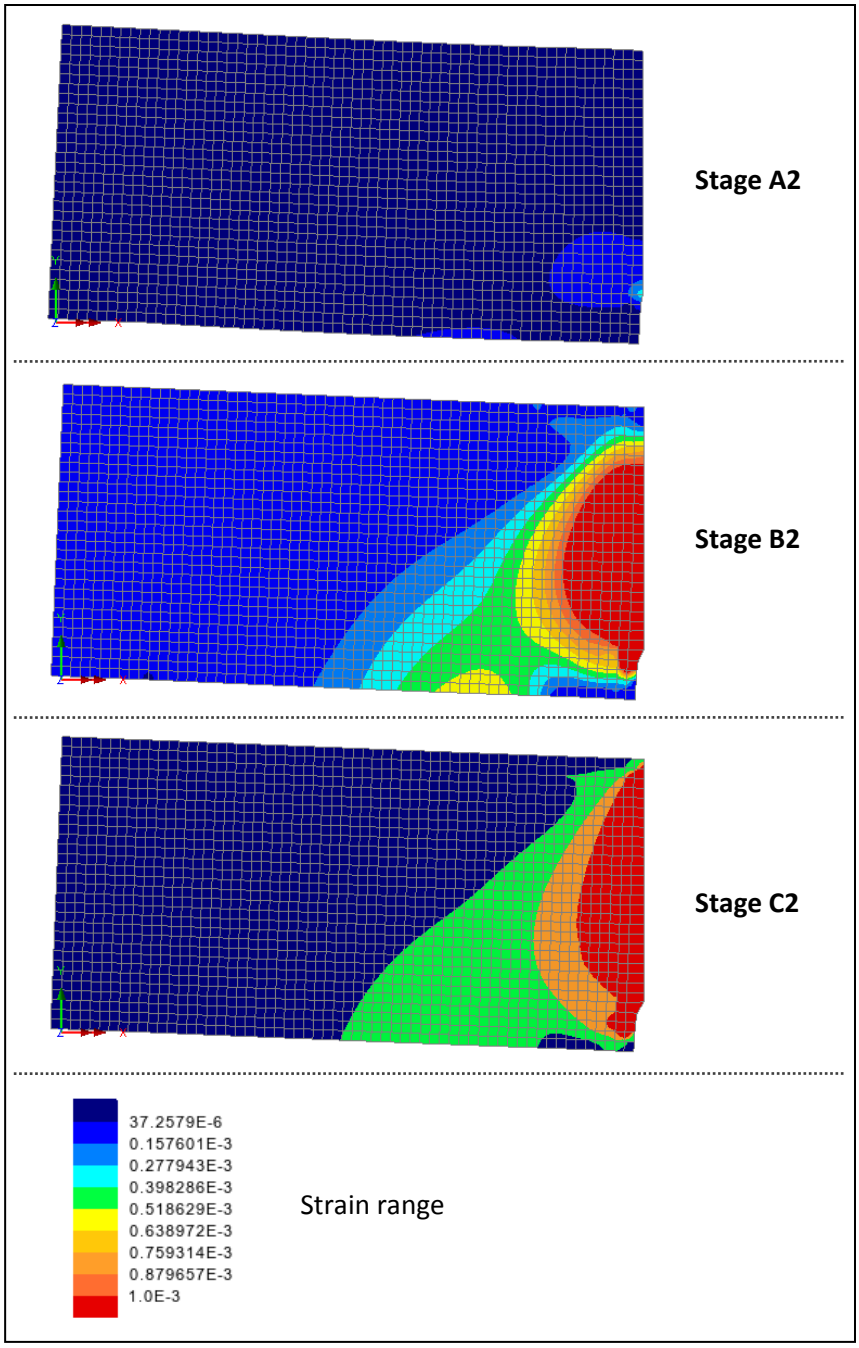

Figure 13b. Major principal strain from FE simulations. V_f = 2%

6.4. FE simulation. 4 point bend test of an FRC beam with additional conventional reinforcement. Flakk and Tordall [48]

The final example is the analysis of a fibre reinforced concrete beam with and without additional flexural reinforcement tested by Flakk and Tordall [48]. Rectangular beams with different amounts of flexural reinforcement, in addition to the 1% volume fraction of Dramix 65/60 fibres in the concrete mix, were tested in 4-point bending. Three series of tests, in which the quantity of flexural reinforcement varied, were carried out and in each of these series two beams were cast and tested. The concrete used was a self compacting concrete designed as a C30. The

test setup is presented in Figure 14 and details of both types of reinforcement are given in Table 8, noting that ϕ12 denotes a standard (high yield, high bond) 12 mm diameter reinforcing bar.

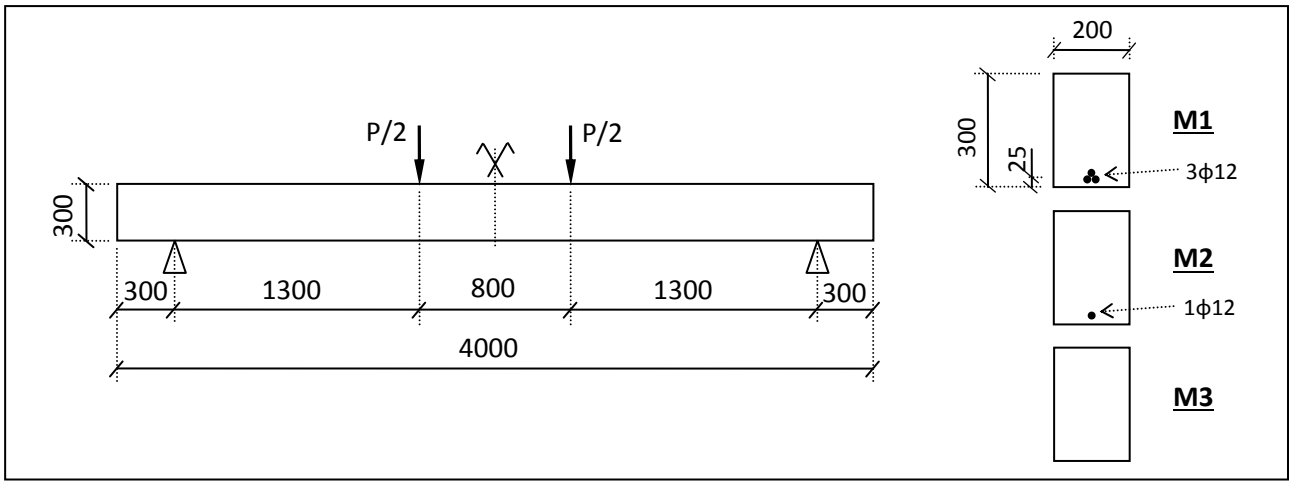

Figure 14. Flakk and Tordall [48] experimental setup

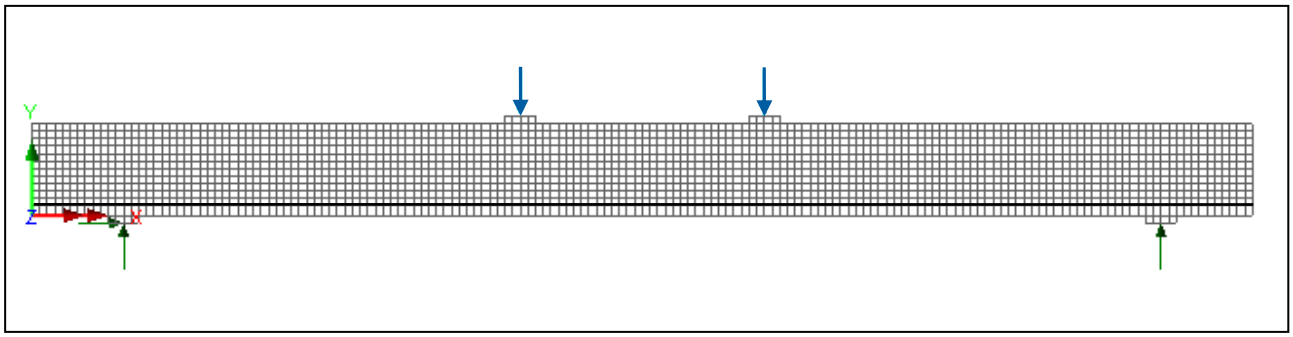

Figure 15. FE mesh and boundary conditions. Flakk and Tordall [48] simulation

Table 8. Material details for series of 4-point bending tests.

Test case	V_f (%)	L_f (mm)	d_f (mm)	Flexural reinforcement
M1	1	60	0.9	3ϕ12
M2	1	60	0.9	1ϕ12
M3	1	60	0.9	-

The finite element mesh used is presented in Figure 15 and the material properties used are given in Tables 9a-c. The reinforcement is modelled with 2D linear bar elements, using a hardening plasticity model for steel with the material properties given in Table 9c.

Finite element predictions of the load – mid-span deflection curves are compared with the experimental curves for the three sets of tests in Figure 16. Plots of the major principal strains showing the regions of localised strains are presented in Figures 17a-c.

Table 9a. Material properties for plain concrete matrix

Case	E_m [MPa]	ν	f_{c0} [MPa]	f_{t0} [MPa]	ε_{c0}	G_f [N/mm]
Concrete matrix	25000	0.2	43	3.2	0.0022	0.1

Table 9b. Material properties for fibres

Case	V_f (%)	L_f (mm)	d_f (mm)	E_f (MPa)	β_f	τ_0 (MPa)	f_{snub}
Fibres	1	60	0.9	210000	0.03	2.75	0.8

Table 9c. Material properties for steel reinforcement

Case	E_s [MPa]	ν_s	f_y [MPa]	H' [MPa]	ε_m
Steel rebars	205000	0.3	580	1000	0.011

f_y=yield stress, H' =hardening modulus, ε_m= the strain limit for hardening

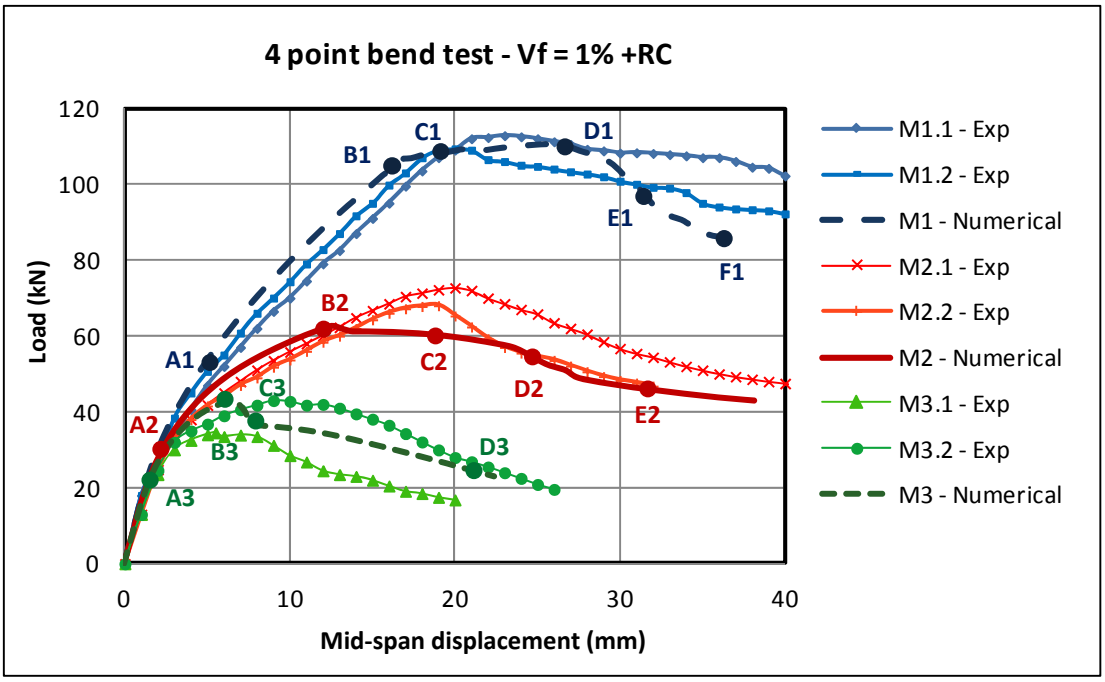

Figure 16. Load-displacement predictions. FE simulations of Flakk and Tordall [48] test

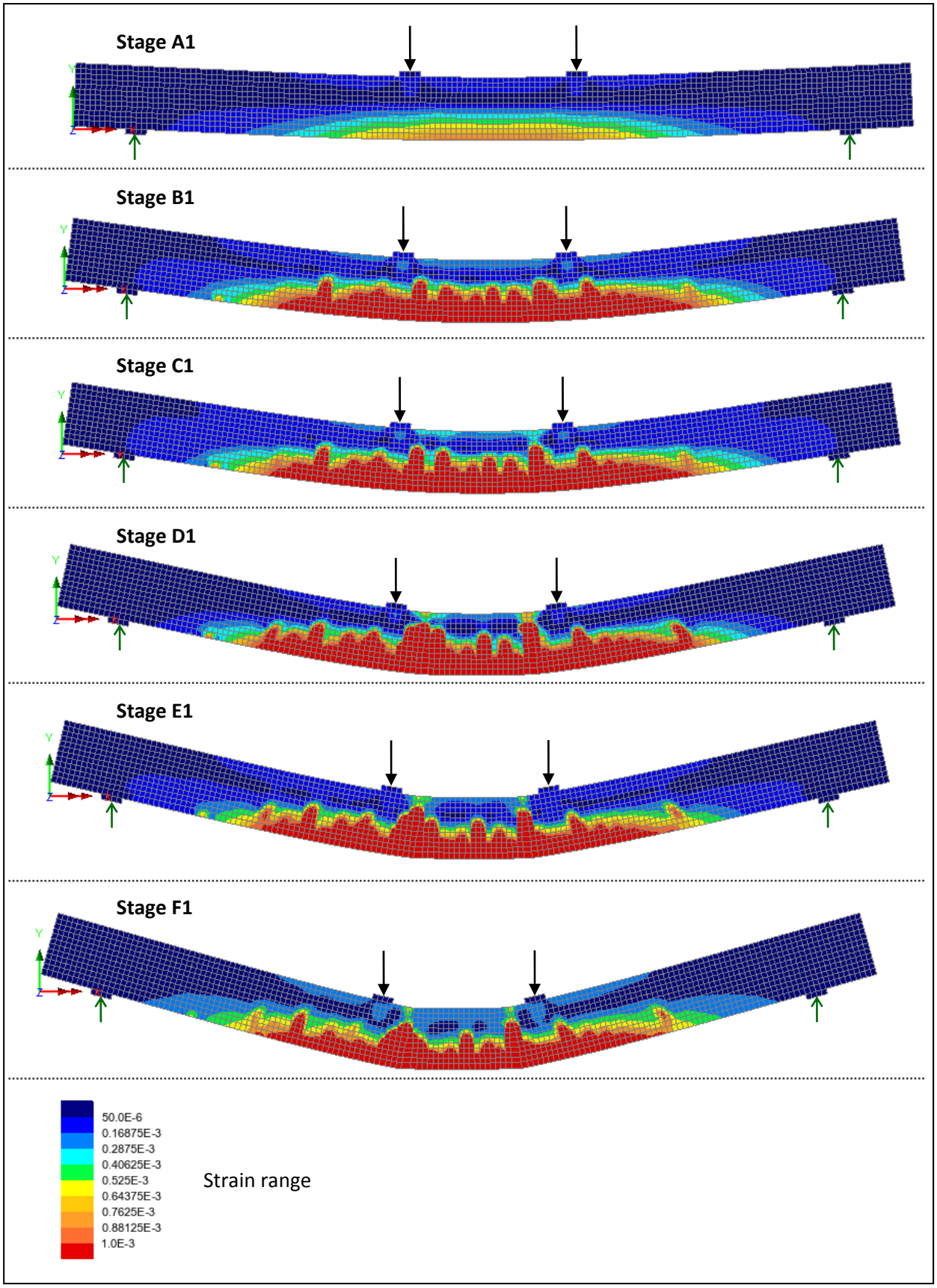

Figure 17a. Principal strain profiles from FE simulations. Set M1

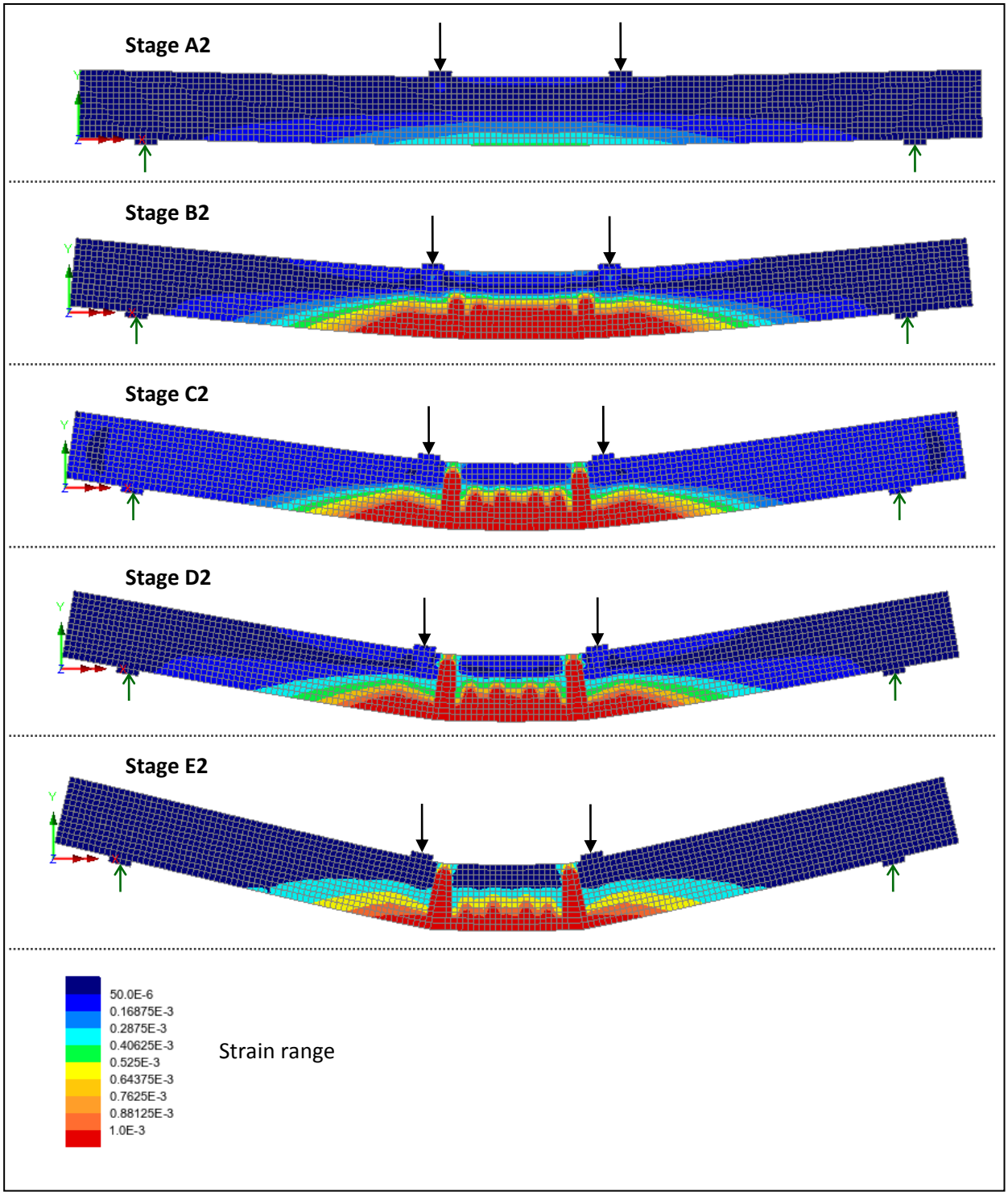

Figure 17b. Strain profiles from FE simulations. Set M2

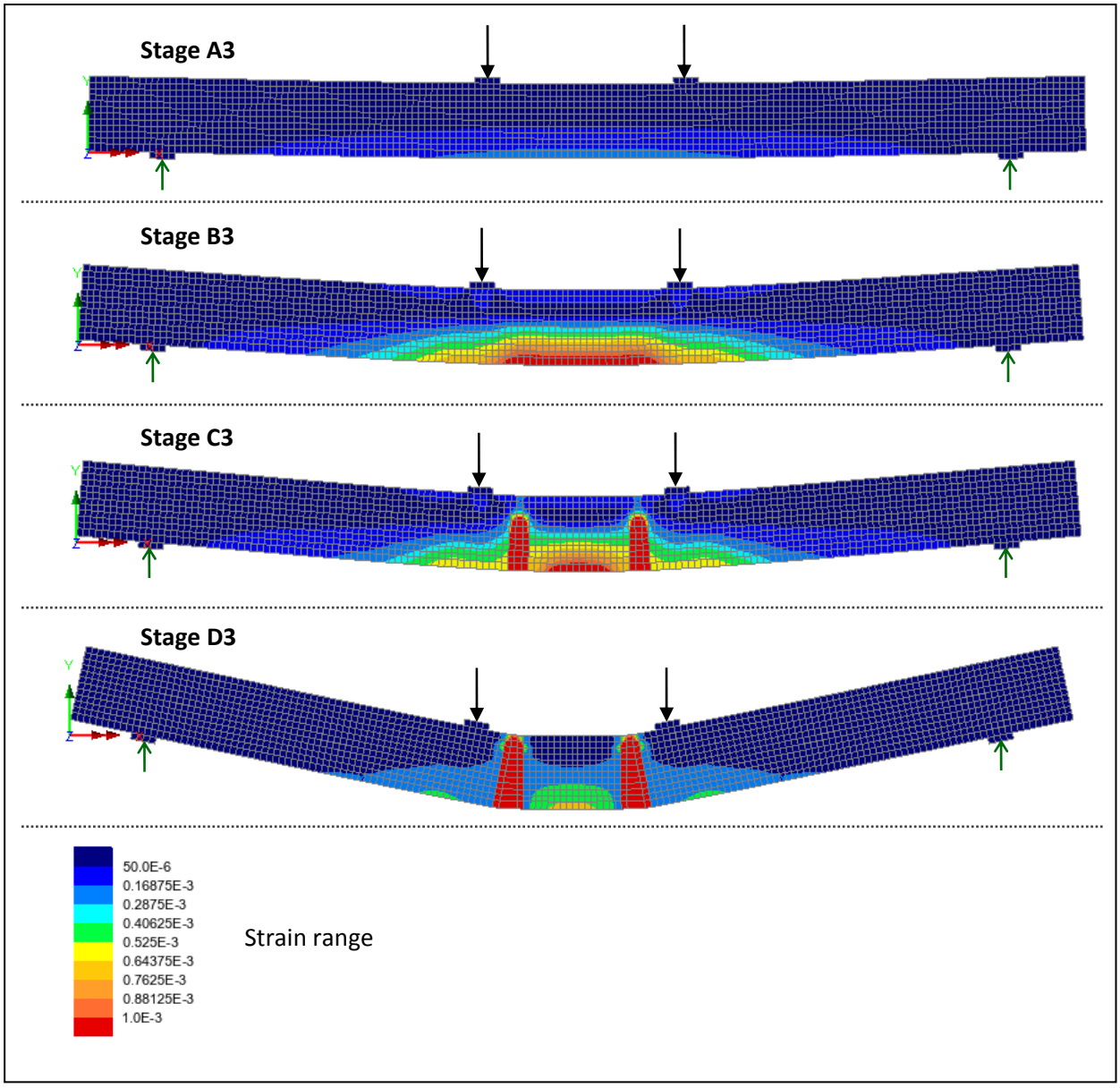

Figure 17c. Strain profiles from FE simulations. Set M3

FE simulations using the proposed model capture well the increase of the peak load and ductility with increasing amount of longitudinal reinforcement. The strain profiles obtained from the simulations of the three tests show that the damage tends to be more distributed the more flexural reinforcement is used which is consistent with experimental observations.

Additionally, load – deflection FE predictions are presented in Figure 18 for the case of a plain concrete beam with conventional flexural reinforcement (RC) and that of an FRC beam with conventional flexural reinforcement (R/FRC) respectively, noting that no such comparisons were provided in the experimental study of Flakk and Tordall [48]. Beam dimensions, FE meshes, boundary conditions and material properties used are those in example M1 (Table 8, 9 and Figures 14, 15), with the exception that $V_f = 0\%$ for the RC case. Comparative plots of the major principal strains for a mid-span deflection of 35 mm are presented in Figure 19 for the two cases.

It can be observed that the addition of fibres to concrete reinforced with conventional reinforcing bars increases the amount of tension-stiffening and the flexural capacity of the

material compared to plain RC. Moreover, the comparative strain profiles in Figure 19 show that cracking is more extended and crack localization is more pronounced in the absence of fibres, suggesting that the cracking characteristics are improved in the case of R/FRC. The qualitative observations drawn from the comparative numerical study are in agreement with the experimental observations of Deluce and Vecchio [49].

When fibres and conventional reinforcing bars are both present, the effect of the fibres can be minimal after the reinforcement has yielded and the crack widths have become sufficiently large for the fibres to fully (or almost fully) pull out. It is noted that, the model automatically accounts for this behaviour as a result of the mechanics based pull-out model. This is apparent in Figure 18 where softening appears soon after the conventional reinforcement yields.

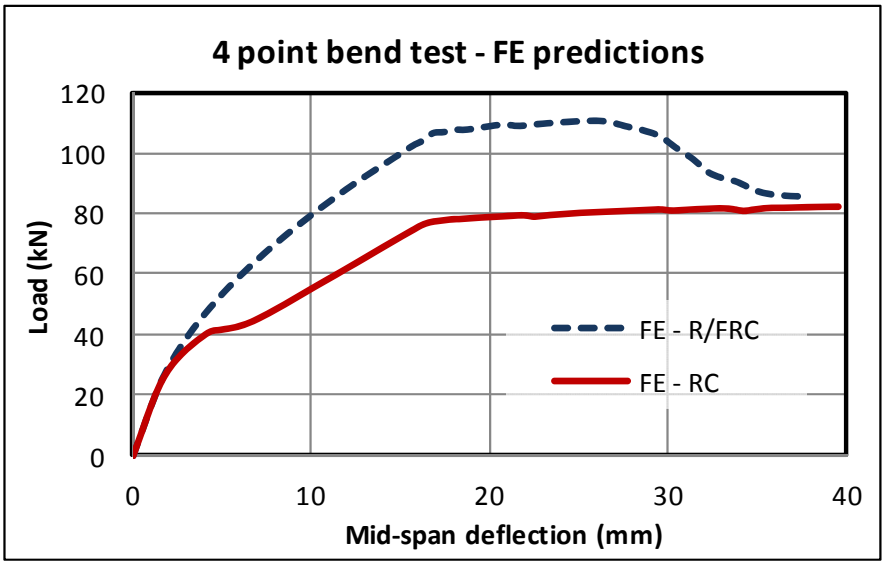

Figure 18. FE predictions for RC and R/FRC beams under 4 point bending

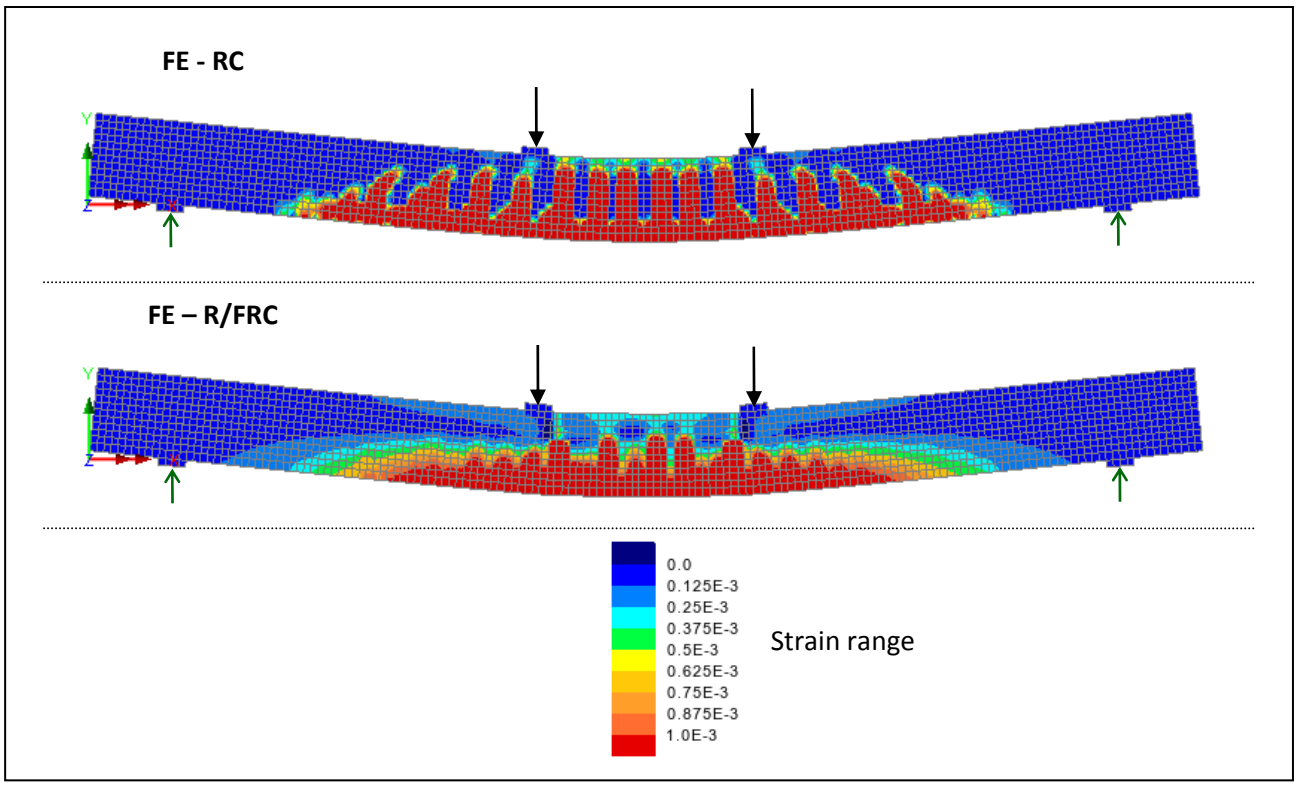

Figure 19. Comparative study. Strain profiles from FE simulations

6.5. Discussion

In general, experimental studies on fibre reinforced cementitious composites show a considerable variability in the behaviour and this is largely attributed to a poor control of the fibre distribution which results in uneven orientations of fibres in different specimens [11, 46]. Significant effort has been directed towards engineering the mix and casting processes for such composites in order to obtain uniform distributions and orientations of fibres [50-52]. However, this statistical variation remains an important factor that should be taken into account when assessing modelling capabilities. Considering the above, a strong correlation between the numerical predictions and experimental results can be observed. This indicates that the proposed model captures correctly key characteristics of the overall macroscopic mechanical behaviour of fibre reinforced cement based composites, such as the increase of ductility and overall toughness of the fibre reinforced composite relative to plain concrete.

No significant numerical instabilities were encountered during the finite element simulations and convergence was achieved for all numerical simulations. The example presented in section 6.3 is used for a convergence study in which the effect of varying the fibre content on the solution convergence history is evaluated. The convergence history for the range of increments that require the largest number of iterations to achieve convergence is presented in Table 10 for V_f = 0% (i.e. plain concrete) and for V_f = 2% respectively. In both cases and the same fixed displacement increment is prescribed. It was found that fewer iterations are required to achieve convergence in the case of fibre reinforced concrete than in the case of plain concrete and therefore the fibre bridging component has a stabilising influence on the model.

Table 10. Convergence history for selected increments

Plain concrete (V_f = 0%)			FRC (V_f =2%)		
Increment	Iteration	Ψ_f(%)	Increment	Iteration	Ψ_f(%)
3	1	5.09E+00	3	1	3.68E+00
3	2	4.54E+00	3	2	2.57E+00
3	3	4.92E+00	3	3	1.72E+00
3	4	4.17E+00	3	4	7.62E-01
3	5	3.67E+00	3	5	4.53E-01
3	6	3.65E+00	3	6	2.91E-01
3	7	3.31E+00	3	7	1.93E-01
3	8	2.47E+00	3	8	3.18E-03
3	9	8.60E-02			
3	10	7.55E-04			
4	1	5.54E+00	4	1	2.62E+00
4	2	6.19E+00	4	2	2.57E+00
4	3	5.30E+00	4	3	1.67E+00
4	4	4.89E+00	4	4	9.73E-01
4	5	4.55E+00	4	5	4.93E-01
4	6	4.06E+00	4	6	2.87E-01
4	7	3.82E+00	4	7	1.82E-01
4	8	3.11E+00	4	8	3.31E-03
4	9	8.16E-02			
4	10	7.64E-04			
5	1	5.54E+00	5	1	1.92E+00
5	2	5.82E+00	5	2	2.94E+00
5	3	5.22E+00	5	3	3.00E+00
5	4	4.76E+00	5	4	1.68E+00
5	5	3.96E+00	5	5	1.23E+00
5	6	3.50E+00	5	6	9.57E-01
5	7	2.98E+00	5	7	3.13E-01
5	8	2.10E+00	5	8	8.66E-03
5	9	5.03E-02			
5	10	3.13E-04			

A mesh convergence study was carried out for the three-point bending example in Section 6.3. A coarse and a fine mesh, with element sizes of 10mm and 5mm respectively, were employed for this purpose (Figure 20). The predicted FE load-deflection responses obtained with the two meshes for V_f = 2% are shown in Figure 21, noting that the parameters in Tables 7a and 7b, case DS2%, were employed in both simulations.

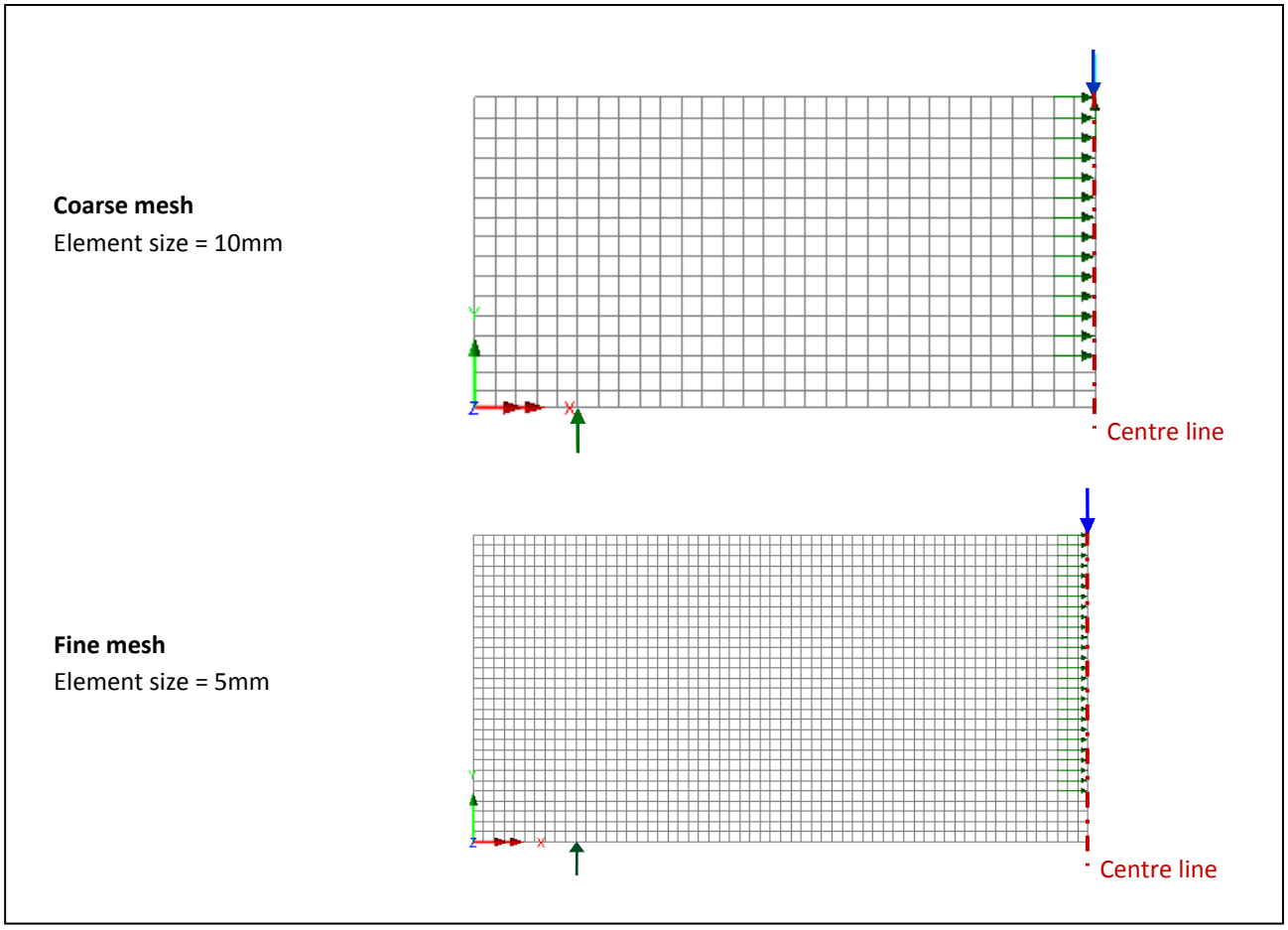

Figure 20. Finite element meshes

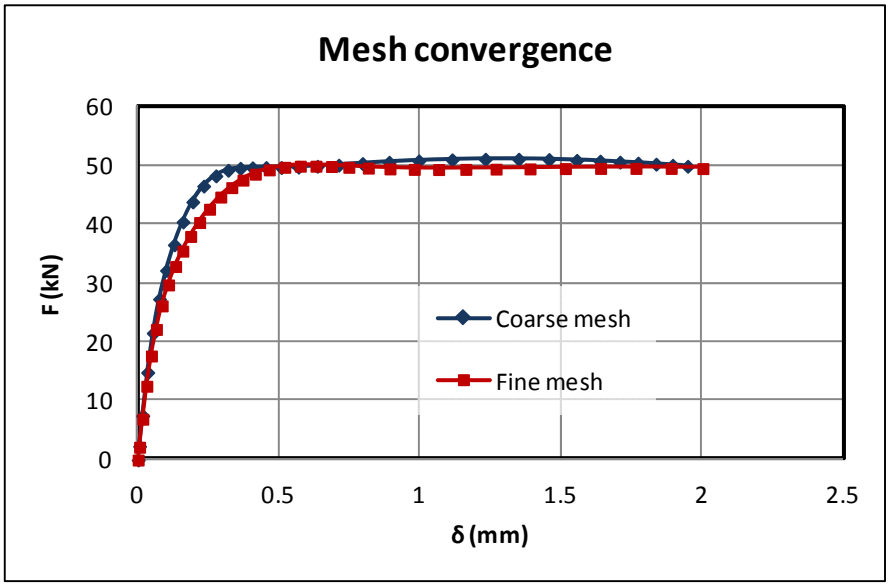

Figure 21. Force – displacement numerical predictions

7. Conclusions

The plastic-damage-contact constitutive model presented is able to simulate directional cracking, rough crack contact and the crack-bridging action of fibres, as well as the increase in fracture toughness and tensile strength that occurs with increasing fibre content. The variation of compressive strength and strain at peak stress with fibre dosage can be modelled using a frictional hardening plasticity component with fibre-content dependent evolution functions.

Numerical predictions, obtained in a range of single-point simulations, show that the proposed model is able to represent well the complex characteristic behaviour of FRC in both tension and compression.

Results from a series of analyses of experimental FRC beams, with and without conventional reinforcement, demonstrate that the constitutive model, when implemented in an FE code, is able to reproduce the experimentally observed behaviour with good accuracy.

Acknowledgements

We would like to thank Technology Strategy Board for supporting this work via the joint Knowledge Transfer Partnership project (KTP 8380) between Cardiff University and LUSAS.

Appendix A. Damage function

The evolution of the damage parameter ω is governed by an effective damage strain parameter ζ and is based on a standard exponential tensile softening function given by:

$$\omega(\zeta) = 1 - \frac{\zeta_t}{\zeta} e^{-c_1\left(\frac{\zeta - \zeta_t}{\varepsilon_0}\right)} \tag{A1}$$

where $\zeta_t = f_{t0}/E_m$ *and* f_{t0} is the uniaxial tensile strength of plain concrete. ε_0 is the strain at the effective end of the uniaxial tensile softening curve and c_1 =5.

The evolution of the effective strain parameter ζ is governed by the following damage function, which is taken from Reference [30];

$$\zeta_{eq}(\tilde{\boldsymbol{\varepsilon}}, \zeta) = \frac{\tilde{\varepsilon}_1}{2}\left[1 + \left(\frac{\mu}{\gamma}\right)^2\right] + \frac{1}{2\gamma^2}\sqrt{\left(\gamma^2 - \mu^2\right)^2 \tilde{\varepsilon}_1^{\,2} + 4\gamma^2\left(\tilde{\varepsilon}_2^{\,2} + \tilde{\varepsilon}_3^{\,2}\right)} \tag{A2}$$

$$\phi_d(\tilde{\boldsymbol{\varepsilon}}, \zeta) = \zeta_{eq}(\tilde{\boldsymbol{\varepsilon}}, \zeta) - \zeta \tag{A3}$$

with the standard loading/unloading conditions $\dot{\zeta} \geq 0; \quad \phi_d \leq 0; \quad \dot{\zeta} \cdot \phi_d = 0; \quad \dot{\zeta}\dot{\phi}_d = 0 \quad \forall \quad \phi_d = 0$

Also, $\zeta = \int_t \dot{\zeta} dt$; in which the superior dot denotes the time derivative and t represents time.

The constants γ and μ are the strain equivalents of the shear stress intercept and the asymptotic shear friction factor respectively of the damage surface in strain space. These are computed from the relative shear stress intercept ($r_\sigma = c/f_{t0}$) and the asymptotic friction factor (μ_σ); i.e. $\gamma = (E/G) \cdot r_\sigma$ and $\mu = (E/G) \cdot \mu_\sigma$; noting that c is the shear stress intercept. R_σ and μ_σ are set to 1.25 and 8 respectively.

If applied to an interface, damage is initiated when ζ_{eq} first exceeds ζ_t. In a continuum model (Section 5), cracks are initiated using a principal stress criterion and the crack plane first forms in the major principal stress plane.

Appendix B. Details of the plasticity model

The yield function F and the plastic potential function G were kept unchanged from the original plasticity model [30]

$$F(\boldsymbol{\sigma},Z(\kappa)) = \sqrt{J_2}\cdot A_r(\theta) + \left(\alpha + \frac{\gamma}{3}\right)\cdot I_1 \cdot \mathrm{Z} - f_c \cdot \mathrm{Z}\cdot(1-\alpha) \tag{B1}$$

$$G(\boldsymbol{\sigma},Z(\kappa)) = \sqrt{J_2}\ A_r(\theta) + \left(\alpha + \frac{\gamma}{3}\right) I_1\ \mathrm{Z}\,\psi - f_c\ \mathrm{Z}\,\psi\ (1-\alpha) \tag{B2}$$

where $A_r(\theta) = \rho_c \left(\frac{2\cos(\theta)^2 + b^2}{\cos(\theta) + \mathrm{b}\sqrt{2\cos(\theta)^2 + c}} \right)$. I_1 = 1st stress invariant, J_2 = 2nd deviatoric stress invariant, θ is the Lode angle (with range 0 to 60°) and Z is a friction hardening factor, which is in turn a function of the work hardening parameter κ. Z varies from a possible value of 0, at which the yield surface degenerates to a line on the hydrostatic axis, up to 1 at the peak surface position. The initial position of the yield surface is governed by the initial value of $Z=Z_0$ which was set to 0.85 for all examples presented here. f_c in Eqs. (B1) and (B2) is the compressive strength that varies with the volume fraction of fibres, as presented in Section 4.

The material parameters required to define the constants are discussed in [30]:

$$\alpha = \frac{b_r - 1}{2b_r - 1}, \quad b = \sqrt{2} - 1, \quad c = \frac{5}{2} - 2\sqrt{2}, \quad \rho = 1/\sqrt{2}, \quad \gamma = \frac{3(1-\rho)}{2\rho - 1}, \quad \rho_c = \sqrt{3} + \frac{\gamma}{\sqrt{3}}$$

in which b_r is the ratio between the uniaxial and biaxial strengths for plain concrete, generally in the range 1.05-1.3 [53,54]. For all examples presented here b_r was set to 1.15.

The plastic potential function *G* has the same form as the yield function with the exception of the addition of the dilatancy term, ψ. ψ is a material parameter which normally set to -0.1 (See Reference [30] for thermodynamic restrictions).

The flow rule is derived from the plastic potential in the standard way as follows

$$\dot{\boldsymbol{\varepsilon}}_{\mathrm{p}} = \frac{\partial \mathrm{G}}{\partial \boldsymbol{\sigma}} \dot{\lambda}_{\mathrm{pl}} \tag{B3}$$

λ_{pl} is the plastic multiplier, which obeys the condition $\dot{\lambda}_{\mathrm{pl}} \geq 0$ and $\dot{\boldsymbol{\varepsilon}}_{\mathrm{p}}$ is the plastic strain rate.

The work hardening parameter, expressed in rate form, is given by:

$$\dot{\kappa} = X(\boldsymbol{\sigma})\boldsymbol{\sigma}^T \dot{\boldsymbol{\varepsilon}}_p \tag{B4}$$

in which $X(\boldsymbol{\sigma})$ is ductility parameter which depends upon the first stress invariant as follows:

$$\begin{aligned} &X = e^{\chi} + e^{\chi - 1} + X_I \\ &where \quad \chi = \frac{I_1}{f_c * 0.9} + 0.55 \ \ and \ \ X_I = 0.0022 \end{aligned} \tag{B5}$$

Appendix C. Consistent tangent matrix with plasticity component active

The consistent tangent matrix with the plasticity component active takes the following form:

$$\delta\boldsymbol{\sigma} = \left[\mathbf{A}_{\mathrm{c}} - \frac{\mathbf{A}_{\mathrm{c}}\mathbf{g}_{\mathrm{m}}\mathbf{f}_{\kappa}{}^{\mathrm{T}}\mathbf{A}_{\mathrm{c}}}{\mathbf{f}_{\kappa}{}^{\mathrm{T}}\mathbf{A}_{\mathrm{c}}\mathbf{g}_{\mathrm{m}} - h_{\kappa}} \right] \delta\boldsymbol{\varepsilon} \tag{C1}$$

in which:

$$\mathbf{A}_{c} = \left(\mathbf{I} + \mathbf{D}_{e} \left(\Delta\lambda \mathbf{G}_{2\sigma\kappa} + \sum_{j=1}^{n} \mathbf{N}_{j}{}^{\mathrm{T}} \tilde{\mathbf{C}}_{j}' \mathbf{N}_{j} \right) \right)^{-1} \mathbf{D}_{e} \tag{C2}$$

$$\mathbf{f}_{\kappa} = \frac{\partial F}{\partial \boldsymbol{\sigma}} + \frac{\partial F}{\partial \kappa} \mathrm{a}_{\kappa} \Delta\lambda \mathbf{k}_{\sigma} \tag{C3}$$

$$\mathbf{g}_{\mathrm{m}} = \frac{\partial G}{\partial \boldsymbol{\sigma}} + \Delta\lambda \frac{\partial^{2} G}{\partial \boldsymbol{\sigma} \partial \kappa} \mathrm{a}_{\kappa} \mathrm{c}_{\kappa} \tag{C4}$$

$$h_{\kappa} = \frac{\partial F}{\partial \kappa} \mathrm{a}_{\kappa} c_{\kappa} \tag{C5}$$

where $\Delta\lambda$ is the increment of the plastic multiplier and:

$$\mathbf{G}_{2\sigma\kappa} = \left(\frac{\partial^{2} \mathrm{G}}{\partial \boldsymbol{\sigma}^{2}} + \frac{\partial^{2} \mathrm{G}}{\partial \boldsymbol{\sigma} \partial \kappa} \mathrm{a}_{\kappa} \Delta\lambda \mathbf{k}_{\sigma}{}^{\mathrm{T}} \right) \tag{C6}$$

$$\mathrm{a}_{\kappa} = \left(1 - \Delta\lambda \mathrm{X} \boldsymbol{\sigma}^{\mathrm{T}} \frac{\partial^{2} \mathrm{G}}{\partial \boldsymbol{\sigma} \partial \mathrm{d}\kappa} \right)^{-1} \tag{C7}$$

$$\mathrm{c}_{\kappa} = \mathrm{X} \boldsymbol{\sigma}^{\mathrm{T}} \frac{\partial \mathrm{G}}{\partial \boldsymbol{\sigma}} \tag{C8}$$

$$\mathbf{k}_{\sigma} = \mathrm{X} \left(\frac{\partial \mathrm{G}}{\partial \boldsymbol{\sigma}} + \frac{\partial^{2} \mathrm{G}}{\partial \boldsymbol{\sigma}^{2}} \boldsymbol{\sigma} \right) \tag{C9}$$

List of symbols

Symbol	Meaning		Symbol	Meaning
$a_c,\ c_{c1},\ c_{c2}$	Constant in hardening plasticity function		$\alpha,\gamma,\rho,\ \rho_c$	Yield function constants (App B)
$a_f,\ a_{f0},\ a_{f\,lim}$	Aspect ratio of fibres and upper & lower limits of this ratio		α_p	Pull-out reduction coefficient (Eq. 10b)
$A_r(\theta)$	Function in plastic yield function (App B)		β_f	Fibre-matrix interface parameter. Frictional sliding hardening parameter
b,c	Yield function constants (App B)		ε_0	Strain at the effective end of softening curve
b_r	Biaxial to uniaxial compressive strength ratio		$\varepsilon_{c0},\ \varepsilon_c$	Strain at uniaxial peak compression for plain concrete and FRC
c	Shear stress intercept (App A)		$\tilde{\varepsilon}_{0\,d}\,,\tilde{\varepsilon}_{0\,p}$	Strains at the end of debonding and pull-out respectively
c_1	Softening curve constant (App A)		$\boldsymbol{\varepsilon},\boldsymbol{\varepsilon}_e,\boldsymbol{\varepsilon}_p$	Cartesian total strain, elastic strain and plastic strain vectors (6x1)
$c_f,\ g$	Constants in the crack-bridging stress function		$\tilde{\boldsymbol{\varepsilon}},\tilde{\boldsymbol{\varepsilon}}_e\ \breve{\boldsymbol{\varepsilon}}$	Crack plane total strain, crack plane elastic strain, crack plane inelastic (or fracture) strain vectors (3x1)
$c_{v1},c_{v2},c_{a1},c_{v\varepsilon 1},$ $c_{v\varepsilon 2},\ c_{v\varepsilon 3},\ c_{a\varepsilon 1}$	Plasticity parameters (Table 2)		$\tilde{\boldsymbol{\varepsilon}}_c$	$\omega\tilde{\mathbf{e}}_c$
$\tilde{\mathbf{C}}$	Elastic crack-band compliance matrix		ζ	Effective damage strain parameter
$\tilde{\mathbf{C}}_{dfs}$	Local crack compliance		ζ_f	Effective crack opening strain parameter
d_f	Diameter of fibres		ζ_t	f_{t0}/E_m (tensile strain measure)
$\tilde{\mathbf{D}}$	Local elastic constitutive matrix		Z_0	Initial value of fraction hardening parameter (App B)
$\boldsymbol{D}_e$	Elasticity tensor matrix		$Z(\kappa)$	Friction hardening/softening function (App B)
$\tilde{\mathbf{e}}_c$	Local embedment strain		$\eta,\eta_\varepsilon,\ \sigma_0$	Constant in the crack-bridging stress function
$E,\ E_f,\ E_m$	Young's modulus of FRC, of fibres and of plain concrete matrix respectively		η_c	Normalised plastic work hardening function
E_{sf}	Effective elastic stiffness of the fibres crossing a crack plane		$\eta_a,\ \eta_v$	Normalised fibre aspect ratio and fibre volume fraction
f_{c0},f_c	Uniaxial compressive strength of plain concrete and of FRC		θ	Lode angle (App B)
f_{t0}	Uniaxial tensile strength of plain		κ	Work hardening parameter (App B)

	concrete			
f_{snub}	Snubbing coefficient		κ_p	κ at peak of control function
$F(\boldsymbol{\sigma},Z)$	Yield function (App B)		λ, Ω	Constant in the crack-bridging stress function
G	Shear modulus (App A)		λ_{pl}	Plastic parameter (App B)
$G(\boldsymbol{\sigma},Z)$	Plastic potential (App B)		$\lambda_v(V_f)$, $\lambda_{v\varepsilon}(V_f)$ $\lambda_a(a_f)$, $\lambda_{a\varepsilon}(a_f)$	Functions describing the variation of f_c and ε_c with V_f and a_f
G_f	Fracture energy		μ μ_σ	Asymptotic shear strain friction factor (App A) Asymptotic shear stress friction factor (App A)
h	Physical crack-band thickness, which equals the width of the fracture process zone		ν	Poisson's ratio
H_c	Contact reduction function		ρ, ρ_c	Yield function constants (App B)
$\boldsymbol{I}$	Identity matrix		σ_0	Constant in the crack-bridging stress function
I_1	1st stress invariant (App B)		$\boldsymbol{\sigma}$	Stress vector (6x1)
J_2	2nd deviatoric stress invariant (App B)		$\tilde{\boldsymbol{\sigma}}$	Crack plane stress vector (3x1)
ℓ_{ch}	Element characteristic length		$\tilde{\boldsymbol{\sigma}}_c$	Contact crack plane stress vector
L_f	Length of fibres		τ_0	Fibre-matrix interface parameter. Shear stress at the end of debonding
m_g	Slope of conical part of contact function		$\varphi_{int}(\tilde{\boldsymbol{\varepsilon}})$, $\varphi_c(\tilde{\varepsilon})$	Interlock and closed contact functions
m_{ful}	Multiplier on ε_0 which controls the effective end of a shear contact region		$\phi_d(\tilde{\varepsilon})$	Damage function (surface in local strain space)
$\boldsymbol{N}$	Stress transformation matrix		$\chi(I_1)$	Mean stress function used in computing X (App B)
$\mathbf{r}_1$, $\mathbf{r}_2$, $\mathbf{r}_3$	Crack plane coordinate unit vectors		$X(\chi)$	Confinement ductility function (App B)
r_σ	Relative shear stress (App A)		ψ	Dilatancy constant
$\tilde{u}_{0d}$, $\tilde{u}_{0p}$	Crack-openings at the end of debonding and pull-out stage respectively		ω	Damage parameter ($0 \le \omega \le 1$)
$\tilde{\mathbf{u}}$	Crack plane displacement vector		ω_f	Fibre effective damage parameter ($0 \le \omega_f \le 1$)

$\breve{\mathbf{u}}$	Inelastic component of the crack plane displacement vector			
V_f	Volume fraction of fibres			

REFERENCES

1 Li V.C., Wang Y. And Baker S. (1991) A micromechanical model of tension-softening and bridging toughening of short random finer reinforced brittle matrix composites. *Journal of the Mechanics and Physics of Solids* **39**(5): 607-625

2 Li V.C. (1992) Postcrack scaling relations for fiber reinforced cementitious composites. *ASCE Journal of Materials in Civil Engineering* **4**(1): 41-57

3 Soetens T., Van Gysel A., Matthys S. and Taerwe L. (2013) A semi-analytical model to predict the pull-out behaviour of inclined hooked-end steel fibres. *Construction and Building Materials* **43**: 253-265

4 Naaman A.E., Namur G.G., Alwan J.M. and Najm H.S. (1991a) Fiber pullout and bond slip. I: Analytical study. *ASCE Journal of Structural Engineering* **117**(9): 2769-2790

5 Naaman A.E., Namur G.G., Alwan J.M. and Najm H.S. (1991b) Fiber pullout and bond slip. II: Experimental validation. *ASCE Journal of Structural Engineering* **117**(9): 2791-2800

6 Karihaloo B.L., Wang J. and Grzybowski M. (1996) Doubly periodic arrays of bridged cracks and short fibre-reinforced cementitious composites. *Journal of the Mechanics and Physics of Solids* **44**(10): 1565-1586

7 Lin Z. and Li V.C., (1997) Crack bridging in fiber reinforced cementitious composites with slip-hardening interfaces. *Journal of the Mechanics and Physics of Solids* **45**(5): 763-787

8 Zhan Y. and Meschke G. Analytical model for the pullout behavior of straight and hooked-end steel fibres. *ACSE Journal of Engineering Mechanics* 2014, **140**(12): 04014091

9 Li F. and Li Z., (2001) Continuum damage mechanics based modelling of fiber reinforced concrete in tension. *International Journal of Solids and Structures* **38**:777-793

10 Lange-Kornbak D. and Karihaloo B.L. (1997) Tension softening of fibre-reinforced cementitious composites. *Cement and Concrete Composites* **19**(4): 285-389

11 Bencardino F., Rizzuti L., Spadea G. and Swamy R.N. (2008) Stress-strain behaviour of steel fiber-reinforced concrete in compression. *ASCE Journal of Materials in Civil Engineering* **20**(3): 255-263

12 Soroushian P. and Lee C.D. (1989) Constitutive modelling of steel fiber reinforced concrete under direct tension and compression. *Fibre reinforced cements and concretes, recent developments,* Swamy R.N. and Barr B. eds., 363-375

13 Ezeldin A.S. and Balaguru P.N. (1992) Normal- and high- strength fiber reinforced concrete under compression. *ASCE Journal of Materials in Civil Engineering* **4**(4): 415-429

14 Barros J.A.O. and Figueiras J.A. (1999) Flexural behaviour of SFRC: Testing and modelling. *ASCE Journal of Materials in Civil Engineering* **11**(4): 331-339

15 Nataraja M.C., Dhang N. and Gupta A.P. (1999) Stress-strain curves for steel-fiber reinforced concrete under compression. *Cement & Concrete Composites* **21**: 383-390

16 Fanella D. and Krajcinovic D. (1985) Continuum damage mechanics of fiber reinforced concrete. *ACSE Journal of Engineering Mechanics* 111(8): 995-1009

17 Peng X. and Meyer C. (2000) A continuum damage mechanics model for concrete reinforced with randomly distributed short fibers. *Computers and Structures* **78**: 505-515

18 Luccioni B., Ruano G., Isla F., Zerbino R. And Giaccion G. (2012) A simple approach to model SFRC. *Construction and Building Materials* **37**: 111-124

19 Chanvillard G. (1999) Modelling the pullout of wire-draw steel fibers. *Cement & Concrete Research* **29:**1027-1037

20 Hameed R., Sellier A., Turatsinze A. and Duprat F. (2013) Metallic fiber-reinforecd concrete behaviour: Experiments and constitutive law for finite element modelling. *Engineering Fracture Mechanics* **103**: 124-131

21 Beghini A., Bažant Z.P., Zhou Y., Gouirand O and Caner F.C. (2007) Microplane model M5f for multiaxial behaviour and fracture of fiber-reinforced concrete. *ASCE Journal of Engineering Mechanics* **133**(1):66-75

22 Caner F.C., Bažant Z.P. and Wendner R. (2013) Microplane model M7f for fiber reinforced concrete. *Engineering Fracture Mechanics* **105**:41-57

23 Kholmyansky M.M. (2002) Mechanical resistance of steel fiber reinforced concrete to axial load. *ASCE Journal of Materials in Civil Engineering* **14**(4): 311-319
24 Radtke F.K.F., Simone A. and Sluys L.J. (2010) A computational model for failure analysis of fibre reinforced concrete with discrete treatment of fibres. *Engineering Fracture Mechanics* **77**: 597-620
25 Bolander J.E., Choi S. and Duddukuri S.R. (2008) Fracture of fiber-reinforced cement composites: Effects of fiber distribution.
26 Schauffert E.A. and Cusatis G. (2012) Lattice discrete particle model for fiber-reinforced concrete. I: Theory. *ASCE Journal of Engineering Mechanics* **138**(7): 826-833
27 Schauffert E.A., Cusatis G., Pelessone D., O'Daniel J.L. and BAylot J.T. (2012) Lattice discrete particle model for fiber-reinforced concrete. II: Tensile fracture and multiaxial loading behaviour. *ASCE Journal of Engineering Mechanics* **138**(7): 834-841
28 Kang J., Kim K., Lim Y.M., Bolander J.E. (2014) Modeling of fiber-reinforced cement composites: Discrete representation of fiber pullout. *International Journal of Solids and Structures* **51**(10): 1970–1979
29 Oliver J., Mora D.F., Husepe A.E. and Weyler R. (2012) A micromorphic model for steel fiber reinforced concrete. *International Journal for Solids and Structures* **49**(21): 2990-3007
30 Jefferson A.D. (2003) Craft – a plastic-damage-contact modl for concrete. I. Model theory and thermodynamic considerations. *International Journal of Solids and Structures* **40**: 5973-5999
31 Jefferson A.D. (2003) Craft – a plastic-damage-contact modl for concrete. I. Model implementation with implicit return-mapping algorithm and consistent tangent matrix. *International Journal of Solids and Structures* **40**: 6001-6022
32 Gopalaratnam V.S. and Shah S.P. (1987) Tensile failure of steel fiber-reinforced mortar. *ACSE Journal of Engineering Mechanics* **113**(5): 635-652
33 Li Z., Li F., Chang T.-Y.P., Mai Y.-W. (1998) Uniaxial tensile behaviour of concrete reinforced with randomly distributed short fibres. *ACI Materials Journal* **95**(5): 564-574
34 Bažant Z.P. and Oh B.H. (1983) Crack band theory for fracture in concrete. *Materials and Structures* **16**: 155-177.
35 Garg S.K., Svalbonas V. and Gurtman G.A. (1973) *Analysis of Structural Composite Materials*. Marcel Dekker, Inc. New York
36 Pasa Dutra V.F., Maghous S., Campos Filho A. and Pachero A.R. (2010) A micromechanical approach to elastic and viscoelastic properties of fiber reinforced concrete. *Cement and Concrete Research* **40**: 460-472
37 Soroushian P. and Lee C.D. (1990) Distribution and orientation of fibers in steel fiber reinforced concrete. *ACI Materials Journal*. **87**(5): 433-439
38 Naaman A.E. and Shah S.P. (1976) Pull-out mechanism in steel fiber-reinforced concrete. *Journal of the Structural Division.* ST8. **102**(8): 1537-1548
39 Walraven J.C. and Reinhardt H.W. (1981) *Theory and experiments on the mechanical behavior of cracks in plain and reinforced concrete subjected to shear loading*. Heron 26(1A), Delft, The Netherlands.
40 Jefferson A.D. (2002) A constitutive model for aggregate interlock on formed crack planes. *International Journal of Numerical and Analytical Methods in Geomechanics* **26**: 1-21
41 Mihai I.C. and Jefferson A.D. (2013) A multi-asperity plastic-contact crack plane model for geomaterials. *International Journal for Numerical and Analytical Methods in Geomechanics* **37**:1492-1509
42 Mihai I.C. and Jefferson A.D. (2011) A material model for cementitious composite materials with an exterior point Eshelby microcrack initiation criterion. *International Journal for Solids and Sturctures* **48**(24): 3312-3325
43 Willam K. and Warnke E. (1975) Constitutive model for triaxial behaviour of concrete. *Proceedings of the International Association of Bridge Structure Engineering*, Report 19, Zurich, Switzerland, 1-30
44 Marar K., Eren Ö. and Yitmen İ. (2011) Compression specific toughness of normal strength steel fiber reinforced concrete (NSSFRC) and high strength steel fiber reinforced concrete (HSSFRC).

Materials Research **14**(2): 239-247

45 Li V.C., Wang Y. and Backer S. Effect of inclining angle, bundling and surface treatment on synthetic fibre pull-out from a cement matrix. *Composites* 1990, **21**(2): 132-140

46 Parmentier B., Vandewalle L. and Van Rickstal F. (2008) Evaluation of the scatter of the postpeak behaviour of fibre reinforced concrete in bending: A step towards reliability. *Seventh International RILEM Symposium in Fibre Reinforced Concrete: Design and Applications, Chennai, India*

47 Bencardino F., Rizzuti L., Spadea G. and Swamy R.N. (2010) Experimental evaluation of fiber reinforced concrete fracture properties. *Composites: Part B* **41**: 17-24

48 Flakk Ø. and Tordal K.N. (2012). *Testing of fibre reinforced concrete structures*. Norwegian University of Science and Technology, Trondheim. MSc thesis.

49 Deluce J.R. and Vecchio F.J. (2013) Cracking behavior of steel fiber-reinforced concrete members containing conventional reinforcement. *ACI Structural Journal* **110**(3): 481-490

50 Grünewald S. (2004) Performance-based design of self-compacting fibre reinforced concrete. *PhD Thesis*. Delft University of Technology

51 Ferrara L., Park Y.D. and Shah S.P. (2008) Correlation among fresh state behavior fiber dispersion and toughness properties of SFRCs. *ASCE Journal of Materials in Civil Engineering* **20**: 493-501

52 Stahli P., Custer R. and van Mier J.G.M. (2008) On flow properties, fibre distribution, fibre orientation and flexural behaviour of FRC. *Materials and Structures* **41**:189-196

53 Kupfer H.B., Hilsdorf H.K., Rusch H. Behaviour of concrete under biaxial stresses, *Journal of ACI* 1969; **66**(8): 656-666.

54 van Mier J.G.M. *Fracture processes of concrete,* CRC Press, 1997.